Systematic evaluation of modern density functional methods for the computation of NMR shifts of 3d transition-metal nuclei

Caspar Jonas Schattenberg,[†] Morten Lehmann,[†] Michael Bühl,[‡] and Martin Kaupp*,[†]

†*Technische Universität Berlin, Institut für Chemie, Theoretische Chemie/Quantenchemie, Sekr. C7, Straße des 17. Juni 135, D-10623, Berlin, Germany*

‡*School of Chemistry, Purdie Building, North Haugh, Sekr. C7, Fife KY16 9ST, St Andrews, United Kingdom*

E-mail: martin.kaupp@tu-berlin.de

Abstract

A wide range of density functionals from all rungs of Jacob's ladder has been evaluated systematically for a set of experimental 3d transition-metal NMR shifts of 70 complexes encompassing 12 × ^{49}Ti, 10 × ^{51}V, 10 × ^{53}Cr, 11 × ^{55}Mn, 9 × ^{57}Fe, 9 × ^{59}Co, and 9 × ^{61}Ni shift values, as well as a diverse range of electronic-structure characteristics. The overall 39 functionals evaluated include one LDA, 8 GGAs, 7 meta-GGAs (including their current-density-functional – CDFT – versions), 9 global hybrids, 4 range-separated hybrids, 8 local hybrids, and 2 double hybrids, and we also include Hartree-Fock and MP2 calculations. While recent evaluations of the same functionals for a very large coupled-cluster-based benchmark of main-group shieldings and shifts achieved in some cases aggregate percentage mean absolute errors clearly below 2%, the best results for the present 3d-nuclei set are in the range between 4-5%. Strikingly, the overall best-performing functionals are the recently implemented CDFT versions of two meta-GGAs, namely cM06-L (4.0%) and cVSXC (4.3%), followed by cLH14t-calPBE (4.9%), B3LYP (5.0%), and cLH07t-SVWN (5.1%), i.e. the previously best-performing global hybrid and two local hybrids. A number of further functionals achieve aggregate deviations in the range 5-6%. Range-separated hybrids offer no particular advantage over global hybrids. Due to the overall poor performance of Hartree-Fock theory for all systems except the titanium complexes, MP2 and double-hybrid functionals are unsuitable for these 3d-nucleus shifts and provide large errors. Global hybrid functionals with larger EXX admixtures, such as BHLYP or M06-2X, also perform poorly, and some other highly parameterized global hybrids also are unsuitable. For many functionals depending on local kinetic energy τ, their CDFT variants perform much better than their "non-CDFT" versions. This holds notably also for the abovementioned M06-L and VSXC, while the effect is small for τ-dependent local hybrids and can even be somewhat detrimental to the agreement with experiment for a few other cases. The separation between well-performing and more poorly performing functionals is mainly determined by their results for the most critical nuclei ^{55}Mn, ^{57}Fe, and ^{59}Co. Here either moderate exact-exchange admixtures or CDFT versions of meta-GGAs are beneficial for the accuracy. The overall deviations of the better-performing global or local hybrids are then typically dominated by the ^{53}Cr shifts, where triplet instabilities appear to disfavor exact-exchange admixture. Further detailed analyses help to pinpoint specific nuclei and specific types of complexes that are challenges for a given functional.

1 Introduction

The NMR chemical shifts of transition-metal nuclei have a long history, dating back to some of the very first NMR experiments in the early 1950s, on the ^{59}Co isotope.[1,2] While some of the relevant nuclei are difficult to observe,[3] others are easily accessible, and many of them cover a rather large range of chemical shifts of many thousands of ppm.[2,4] This large range and the importance of transition-metal complexes in many areas of research, from organometallic catalysis via materials to bioinorganic chemistry, makes NMR spectroscopy of transition-metal (TM) nuclei an important tool in chemistry. As with main-group NMR,[5–7] quantum-chemical computations of transition-metal NMR parameters have thus been of substantial interest.[7–13]

One of us (MB) has initiated systematic studies of DFT approaches to compute TM NMR shifts about 25 years ago, with one of the aims being the correlation with reactivity, and an appreciable knowledge base has been accumulated over the years. Apart from structural, environmental, and ro-vibrational effects, the choice of the exchange-correlation (XC) functional has been crucial to obtain reasonable predictive-quality TM NMR shifts. Initially, (global) hybrid functionals (GHs) with a moderate admixture of Hartree-Fock exchange, such as the B3LYP functional (20%), were found to improve the obtained shifts for many TM nuclei, compared to pure semi-local functionals. This holds in particular for nuclei in the second half of the 3d series, such as ^{57}Fe or ^{59}Co,[14–16] to a lesser extent also for ^{55}Mn,[17] ^{61}Ni,[18] and for some late 4d nuclei, ^{99}Ru and ^{103}Rh.[15,19–21] Different rationalizations can be put forward for these observations. Delocalization errors of semi-local functionals are known to render metal-ligand bonds too covalent, as also shown for EPR parameters of open-shell complexes.[22,23] Potentially too low excitation energies of semi-local functionals and the coupling terms introduced by nonlocal exchange are additional aspects.[24] Later, studies for some 4d nuclei such as ^{95}Mo or ^{99}Tc,[25,26] or for the 3d nucleus ^{53}Cr,[27] suggested better performance of semi-local functionals and detrimental effects of exact-exchange (EXX) admixture for such elements in the middle of the TM rows. Relatively small dependencies on the EXX admixtures were identified for early TMs, such as ^{49}Ti, ^{51}V or ^{91}Zr.[28–30]

Many results for main-group nuclei also suggest that different amounts of EXX admixture of global hybrids may

be preferable for different nuclei. For example, the BHLYP functional with 50% EXX admixture has been suggested[31] to be among the best choices for ^{19}F shifts (double hybrid functionals - DHs - like DSD-PBEP86 perform even better,[32] but these require computationally demanding MP2-type correlation contributions and have similarly high EXX admixtures). On the other hand, BHLYP dramatically overestimates chemical shifts for many other main-group nuclei[33,34] (and for transition metals,[35] see also below). Indeed, it appears that the optimal amount of EXX admixture depends not only on the nucleus studied but also on the electronic structure of the given compound. That is, large EXX admixtures are known to be problematic in many cases exhibiting large static correlation contributions and in case of triplet instabilities of the generalized ground-state Kohn–Sham wave function.[36,37] This brings us back to the main topic of transition-metal compounds, which are known to often exhibit large static correlation effects as well as spin-symmetry breaking of Hartree-Fock wave functions, depending on oxidation and charge state, as well as on other characteristics of their electronic structure.

In view of these limitations of global hybrid functionals in terms of their flexibility of being able to treat different situations, more flexible extensions of the concept of hybrid functionals obviously are of interest, not exclusively but distinctly also in the context of NMR chemical shifts. So far, the use of range-separated hybrids (RSHs) has been studied to a limited degree, and the results did not seem to provide a significant improvement over global hybrids. This brings us to local hybrid functionals (local hybrids, LHs) with position-dependent EXX admixture, governed by a so-called local mixing function (LMF).[38] An early attempt to use LHs for nuclear shieldings based on an uncoupled scheme on top of an approximate optimized-effective-potential (OEP) treatment within the localized-Hartree-Fock (LHF) approach[39] suffered from the sensitivity of nuclear shieldings to the underlying approximations used.[40,41] Recently we have reported a full and efficient coupled-perturbed Kohn-Sham (CPKS) implementation of nuclear shieldings with LHs within the Turbomole code, based on generalized Kohn-Sham ground-state wave functions.[33] The first evaluations for main-group nucleus shieldings of some first-generation LHs were very encouraging, confirming the potential advantages of having large EXX admixtures in the core region but lower ones in the valence region. In particular, the systematic underestimate of shieldings by semi-local or global hybrid XC functionals for non-hydrogen nuclei, which in part seems to be related to the neglect of current terms in the XC functionals,[42] was reduced significantly. Some limitations noted initially for ^{1}H shieldings, and for the shieldings of nuclei in direct neighborhood of hydrogen atoms, were found[43,44] to be related to the gauge correction of the kinetic energy τ by the widely used Maximoff-Scuseria model.[45] They vanish almost completely when using the Dobson[46–49] current-density functional (CDFT) extension of τ.[43] Further improvements for hydrogen shieldings were found[44] when using more advanced LHs with calibrated exchange-energy densities, such as LH20t.[50] Subsequent evaluations of main-group NMR shifts as part of a more diverse evaluation of local hybrids for response properties by Holzer et al.[51] included the same LHs and in addition a modified variant (mPSTS) of the rather involved PSTS functional,[52] as well as an LH (LHJ14) by Johnson and coworkers[53] with an LMF based on correlation length. Good performance of LHs was generally found, even though the selected test sets in part may have been too limited to distinguish the advantages and disadvantages of different functionals in granular detail. To obtain a more meaningful extensive comparison of a wide variety of XC functionals and other methods for main-group shieldings and shifts, we have very recently constructed and used[34] a very large benchmark set containing 372 shielding values for ^{1}H, ^{11}B, ^{13}C, ^{15}N, ^{17}O, ^{19}F, ^{31}P, and ^{33}S nuclei in 117 molecules and ions, based on CCSD(T)/pcSseg-3//CCSD(T)/cc-pVQC data and used it to evaluate a wide variety of different functionals from all five rungs of Perdew's "Jacob's ladder of functionals"[54] plus HF and MP2 calculations. The DSD-PBEP86 DH[55,56] was confirmed to provide the overall most accurate results. Several LHs performed excellently and were competitive with the other DHs evaluated, at appreciably lower computational cost. A number of further important insights were obtained on other functionals. This includes in particular the excellent performance of parameterized meta-GGAs like B97M-V and MN15-L, when used in their CDFT implementations based on Dobson's scheme ("cB97M-V", "cMN15-L").[34]

A more diverse evaluation of XC functionals for NMR shifts clearly should extend beyond main-group nuclei. Many of the functionals mentioned above, that have recently been evaluated in detail for main-group shieldings, have so far not been applied to transition-metal shifts. Here we work towards filling this gap and provide a systematic study of the NMR shifts of 3d nuclei, as more data are available for comparison here than for the heavier TM nuclei, complications due to relativistic effects (or potentially to violations of the high-density limit for certain functionals[57]) are expected to be small, but the potential importance of static correlation is largest. The latter point reflects the often found stretched-bond situations related to the large Pauli repulsion with semi-core shells, exacerbated by the small 3d shell that lacks a radial node.[58,59] We include 70 shifts of ^{49}Ti, ^{51}V, ^{53}Cr, ^{55}Mn, ^{57}Fe, ^{59}Co, and ^{61}Ni nuclei, where experimental data are available. The selection includes complexes that have been studied previously by computations, and we concentrate largely on systems where environmental effects are not expected to affect the shifts very much (see below). As the generation of high-level coupled-cluster benchmark data of comparable quality as provided for main-group systems in Ref. 34 would be prohibitive and might not provide the required accuracy in all cases, we compare here to carefully selected experimental data.

Beyond the first evaluations of LHs for transition-metal NMR shifts, we include some GGAs geared specifically towards nuclear shieldings of main-group nuclei (KT1, KT2, KT3), more recent meta-GGA functionals (e.g. B97M-V, M06-L, MN15-L, VSXC, τ-HCTH), a number of more recent and highly parameterized GHs, and four RSHs (CAM-B3LYP, ωB97X-D, ωB97X-V, ωB97M-V). We also evaluate HF and MP2 calculations and two DHs, B2PLYP and DSD-PBEB86, even though we expected these approaches to face difficulties for many transition-metal complexes where appreciable static correlation and triplet instabilities are common. Yet MP2 and DSD-PBEP86 excel for most main-group shieldings,[34] and so it is only fair to evaluate them also for transition-metal shifts. Overall, 41 methods are evaluated for the entire test set, without counting different ways of treating local kinetic energy, τ. In the Theory section we describe the issue of the proper treatment of τ for those functionals that depend on it,[43,44] as this will turn out to be a major aspect for the success of some of the best-performing

functionals in this work.

2 Theory

As many of the functionals evaluated here, meta-GGAs, meta-GGA-based GHs and RSHs, and LHs with certain local mixing functions (LMFs), depend on local kinetic energy τ, the proper treatment of the latter becomes important and shall be briefly discussed here. τ itself is not invariant to gauge transformations of the vector potential in the presence of a magnetic field and has to be adjusted accordingly. In most nuclear shielding implementations used today, a gauge-invariant extension due to Maximoff and Scuseria[45] is used (τ_{MS} in the following)

$$\tau \longrightarrow \tau_{MS} = \tau + \frac{\mathbf{A}^{\mathrm{T}}}{c}\mathbf{j}_p + \frac{|\mathbf{A}|^2}{2c^2}\rho \tag{1}$$

where

$$\mathbf{j}_p = \frac{i}{2}\sum_i (\varphi_i \nabla \varphi_i^* - \varphi_i^* \nabla \varphi_i) \tag{2}$$

is the paramagnetic current density, and $\mathbf{A}$ is the vector potential of the magnetic field. However, use of the physical current does not generate a proper isoorbital indicator,[47,48] as τ is in the absence of a field, and this treatment renders τ explicitly field-dependent, which is considered theoretically disadvantageous.[49] More importantly, we have found the model to introduce unphysical paramagnetic artifacts for atoms and for the parallel shielding tensor component in linear molecules,[43] which also turned out to be responsible for a poor description of proton shieldings (and for some other artefacts) by first-generation LHs. It is advantageous to use instead the more physically motivated induced paramagnetic current density. This gives a model proposed by Dobson[46] that has been used also in other contexts (e.g. for gauge invariance of τ-dependent functionals in TDDFT computations,[47] to describe current-carrying atomic states[48] or molecules in strong magnetic fields,[60] to study magnetically induced currents,[61] or to compute spin-spin coupling constants[51,62]):

$$\tau \longrightarrow \tau_D = \tau - \frac{|\mathbf{j}_p|^2}{2\rho} \tag{3}$$

Use of τ_D eliminates the abovementioned artifacts of τ_{MS} and provides a proper current-density functional theory (CDFT) framework for τ-dependent XC functionals. This entails coupling terms in the response treatment also for meta-GGA functionals.[43] We will in the following denote these CDFT implementations of the functionals by a small "c" prefix, as has been done in several previous works.[34,51,60,61] We note in passing that in the present linear-response treatment, τ_D applies only to the response terms, while a variational treatment of the magnetic field will also turn the ground-state functionals into CDFT functionals.[60] While both τ_{MS} and τ_D frameworks will be considered in this work, we regard τ_D as the physically better founded one and will place central focus on its results. A gauge-dependent model with an unmodified τ (with the gauge origin placed at the center of mass of the molecule, τ_C), as well as the *ad-hoc* gauge invariant solution implemented in ORCA[63–65] (τ_0; see discussion in Ref. 43) will also be mentioned or reported where we find it useful to discuss the role of current-density dependence in τ_D.

While nuclear shielding is a tensor property, for the purpose of the present work we will concentrate on the isotropic shielding

$$\sigma_{iso} = \frac{1}{3}Tr(\boldsymbol{\sigma}) \tag{4}$$

As no reference-quality computed shielding data are available, in contrast to the main-group case (see Introduction) we will have to compare our results to experimental chemical shifts. The NMR chemical shift is usually reported (approximately) as the difference between the shielding of a reference compound and that of the nucleus of interest

$$\delta = \sigma_{iso,ref.} - \sigma_{iso} \tag{5}$$

In case of transition-metal nuclei and complexes, the choice of reference compound becomes particularly important, as some complexes may be more difficult to compute than others regarding static correlation or environmental effects. To exclude as far as possible artifacts arising from such errors, one can try to use "benign" reference compounds that are comparably easy to compute accurately. In those cases where the choice differs from that made by the experimentalists for a given nucleus, one can map the computed results back to the experimental shift scale by using the experimental shift of the chosen secondary reference standard relative to the experimentally used one

$$\delta = \sigma_{iso,ref.calc.} - \sigma_{iso,calc.} + \delta_{ref.exp.} \tag{6}$$

We will discuss the chosen reference standards at the beginning of the Results section, in comparison with the alternative approach of referencing via the Y-intercept of the linear regression of computed σ_{iso} against experimental δ values at a given computational level.[18] The latter will be our central choice for statistical analyses.

3 Computational Details

All regular DFT calculations (except double hybrid shielding calculations) were carried out with a developers' version of the TURBOMOLE program suite.[66,67] Structures of all complexes were optimized at the BP86-D3(BJ)/def2-TZVP(D)[68,69] level of theory, i.e. using a def2-TZVPD basis for the metal centers and def2-TZVP for the main group atoms, which is similar to the structures used in many earlier transition-metal NMR shift studies.[15–21,28–30] To evaluate the role of the structures for the shift computations, we also evaluated TPSSh-D3(BJ)[70]/def2-TZVP(D) structures for comparison. D3(BJ) represents D3 atom-additive dispersion corrections,[71,72] with Becke-Johnson damping.[73–75] The maximum norm of Cartesian gradients was converged to 10^{-5}, with an energy convergence criterion of 10^{-8}. Grids were set to "5" for BP86 optimizations and to "3" in TPSSh optimizations (internal TURBOMOLE settings). All structures were characterized as true minima by subsequent harmonic vibrational frequency analyses.

Some truncated model complexes, $VOMe_3$, $VOMe_2(OMe)$, $VOMe(OMe)_2$, $VO(OMe)_3$, and $Fe(CO)_4(CH_2CHOMe)$, have been used throughout the present work, while the experimental shifts were reported for the larger $VO(CH_2SiMe_3)_3$, $VO(CH_2SiMe_3)_2(O^tBu)$, $VO(CH_2SiMe_3)(O^tBu)_2$, $VO(O^tBu)_3$, and $Fe(CO)_4(CH_2CHOEt)$.[76,77] To study the effect of the truncation, the full-sized complexes have been optimized by the Conformer-Rotamer Ensemble Sampling Tool (CREST)[78,79] followed by a BP86-D3(BJ)/def2-

TZVP(D) optimization of all relevant conformers. We selected the energetic minimum of this search and evaluated the shielding constants for a small subset of functionals. Comparisons of the results for three functionals are reported in Table S13 in Supporting Information. Changes of the NMR shifts compared to the truncated complexes are below 50 ppm. Relative to the experimental shift scale the changes do not exceed 2.1%, whereas the relative statistical results are affected by a maximum of 0.3% for the evaluated functionals. Due to the small effects on the overall statistics, and to be consistent with previous publications (see Refs. 15,29), we use the truncated models throughout.

DFT shielding calculations with TURBOMOLE used gauge-including atomic orbitals (GIAOs),[80–82] pcSseg-3[83] basis sets, SCF energy convergence criteria of 10^{-9}, a ground-state density convergence of 10^{-7}, and a grid setting "3". Convergence thresholds for the CPKS iterations were set to 10^{-7} (convergence of the Euclidean vectors).

GIAO-CCSD(T)/pcSseg-3 results for some atoms (see Table 1 below) were computed using the CFOUR program.[84] All double hybrid and MP2 GIAO shielding calculations have been performed using the ORCA program, version 4.2.1.[32,63,64] Due to the much larger computational requirements of such computations compared to regular DFT shielding calculations, the basis sets have been reduced somewhat in a locally-dense basis-set approximation to still be able to carry out these calculations for all complexes in reasonable time. pcSseg-3 basis sets were then used only on the transition metal nuclei themselves, while pcSseg-2 basis sets were used on the ligand atoms. The RI approximation (resolution of the identity) has been used employing the def2-universal[85,86] auxiliary basis for the Coulomb and exchange part (RI-JK, AuxJ/AuxJK) and the "AutoAux" option with size setting "1" was used for the auxiliary basis within the MP2 correlation part (AuxC).[87] For one double hybrid (DSD-PBEP86), we have tested the full pcSseg-3 basis set and practically complete auxiliary basis sets (using the "AutoAux" option with setting "3" and the additional setting "AutoAuxLMax=True") for a subset of the smaller complexes. While the differences to the mixed-basis results are non-negligible, they do not affect the overall judgement on the lack of suitability of MP2 and the DHs for the present 3d shift test set (except for ^{49}Ti). Shifts at Hartree-Fock level have also been computed, using both TURBOMOLE and ORCA, with closely similar results.

We do not include thermal corrections or solvent effects in the benchmark statistics. Previous analyses have found the former to be quite small in comparison to the shift ranges of the involved nuclei and possible errors of the XC functionals, and the latter in most cases too,[88,89] at least for the types of complexes studied here. Indeed, larger effects are typically found from possible errors in the optimized structures.[16,90] Exceptionally large solvent influences are expected for some highly charged species in aqueous solution, in particular for nuclei with large shift ranges, due to a shortening of the average metal-ligand distances by the solvent environment. One of us (MB) has investigated this previously for a number of Co complexes from the present test set. Based on snapshots from ab initio MD simulations (CPMD level), or based on polarizable continuum models (PCM), the effects on aqueous $[Co(H_2O)_6]^{3+}$, $[Co(NH_3)_6]^{3+}$, $[Co(CN)_6]^{3-}$, and $[Co(CO)_4]^-$ have been estimated.[91] The shifts of these charged systems are reduced compared to their gas-phase values, which can of course alter the comparison between computational methods and experiment. Table S7 and Figure S2 in Supporting Information show how the statistics for the ^{59}Co subset and those for the entire test set are altered if we consider the two types of correction schemes (PCM vs. CPMD) for the four complexes to back-correct their experimental shifts to obtain approximate gas-phase values. The effects on the individual ^{59}Co subset are indeed non-negligible. Notably, the deviations with several (global, local, and range-separated) hybrid functionals tend to be reduced to some extent, in particular with larger EXX admixtures. The reason is, that many of these functionals, when used in gas-phase calculations, tend to overestimate the large shifts of these charged species. Semi-local functionals tend to benefit much less from the solvent corrections (for cSCAN the CPMD correction even overshoots), while agreement for SVWN is also improved. The overall trends for the different types of functionals remain similar, but a few changes in the order of the best-performing functionals are found (B3LYP becomes now the best-performing functional for the ^{59}Co subset, and several LHs perform similarly well, in particular cLH20t; Table S7). For the combined test set of all nuclei, the changes are small, however, with the largest shifts below 0.5% in rel SDs and below 0.3% in rel. MAEs compared to the uncorrected data (Figure S2). We find even smaller effects of both explicit and implicit solvent modeling for aqueous $Cr_2O_7{}^{2-}$ (Figure S3 and Tables S8 and S9). Another potential source of larger solvent effects could be explicit coordination of donor solvent molecules to unsaturated metal sites. We examined this for a number of complexes for which the experimental data had been taken in the potential donor solvent acetonitrile. But even in cases where the computations suggest solvent coordination, the effects on the metal shifts are very small. Neither solvent effects for the charged complexes in aqueous solution nor explicit solvent coordination to the metal center are large enough to modify our conclusions on the suitability of different electronic-structure methods notably. The tremendous effort of modelling the solvent environment for all relevant species would be clearly outside the scope of the present work

Likewise, no relativistic corrections are included. Scalar relativistic computations using the X2C Hamiltonian[92] have been carried out at the cM06-L level and are provided in Table S12 in Supporting Information. The largest effect on absolute shieldings is ca. 75 ppm, and variations within a given subset are less than 50 ppm. Given the much larger shift ranges covered for each nucleus, these are negligible contributions. At first sight, spin-orbit effects due to heavy ligand atoms might be expected to be significant for complexes like $TiBr_4$. However, due to the small metal s-character in the metal-ligand bonds, these effects should be small.[93–95]

As triplet instabilities are an issue for some of the complexes in case of hybrid functionals with larger EXX admixtures and for Hartree-Fock and MP2, we carried out stability analyses of the wave functions. In TURBOMOLE triplet instabilities can be investigated in the escf module by calculating the lowest eigenvalues of all irreducible representations of the electronic Hessian. In ORCA the keyword "stabperform" was employed for the same purpose. In that case we could also follow the eigenvector associated with the most negative eigenvalue and get unrestricted solutions, in some cases also their shieldings. Instabilities are indicated by red color in the full shielding results in Tables S43 – S55 in Supporting Information. While the instability analyses for the mPSTS LH did also indicate instabilities, we this appears to be to be an artefact of the recent implementation of this functional (see

below) in the analysis rather than true instabilities. We did not pursue UKS solutions for general shielding analyses at a larger scale but report the RKS-based results. However, we did additional analyses of the UKS solutions for the BHLYP functional with 50% EXX admixture to estimate the importance of the symmetry breaking for a method where a larger number of unstable RKS solutions were found (see Section S4 and Table S10 in the Supporting Information). For most complexes studied, the UKS solutions did not show strong symmetry breaking (see S^2 expectation values of zero). For the few cases with spin-broken UKS solutions, somewhat larger deviations are seen, but on a scale that would not affect significantly the overall performance of BHLYP in the statistical evaluations. The same is expected to hold for for other hybrid functionals with similar or lower EXX admixtures, where triplet instabilities are seen. Matters are different for HF and consequently for MP2: here the negative eigenvalues are much larger for a given complex than for BHLYP, and to some extent this holds already for the DSD-PBEP86 DH (Table S11). UHF solutions tend to exhibit large symmetry breaking, and their associated shielding values can be very different from those obtained for the unstable RKS solutions. Consequently we have to consider HF and MP2 results, as well as double-hybrid data, meaningless in many cases, and we keep them in Supporting Information only as an illustration of the failure of these methods. The differences between BHLYP and HF instabilities can be inferred from the magnitude of the negative eigenvalues of the electronic Hessian: these are much smaller with 50% EXX admxiture than for 100% (Table S11). The TURBOMOLE and ORCA stability analyses for HF wave functions do not align to 100%, but this does not affect the main conclusions drawn.

The XC functionals evaluated in the TURBOMOLE shielding and shift calculations include SVWN[96,97] as an example of an LDA functional (rung 1), the rung 2 GGA functionals BLYP,[98,99] BP86,[98,100,101] PBE,[102] KT1,[103] KT2,[103] KT3,[104] B97D[105] and HCTH,[106,107] and the rung 3 meta-GGA functionals TPSS,[108] M06-L,[109] MN15-L,[110] VSXC,[111], τ-HCTH,[112] B97M-V,[113] and SCAN.[114] Global hybrid functionals (GHs, rung 4) include TPSSh,[70] B3LYP,[115] PBE0,[116] B97-2,[117] BHLYP,[118] PW6B95,[119] M06,[120] MN15,[121] and M06-2X.[120] We additionally tested the four range-separated hybrids (RSHs, rung 4) CAM-B3LYP,[122] ωB97X-D,[123] ωB97X-V,[124] and ωB97M-V,[125] as well as the local hybrid functionals (LHs, also rung 4) LH07s-SVWN,[126] LH07t-SVWN,[127] LH12ct-SsirPW92,[128] LH12ct-SsifPW92,[128] LH14t-calPBE,[129] LH20t,[50] mP-STS,[51,52] and LHJ14.[53] LH14t-calPBE and the recent LH20t are the only local hybrids here that include calibrated exchange-energy densities. mPSTS and LHJ14 have been recently implemented into TURBOMOLE by Holzer et al..[51] mPSTS is a slightly modified version of the PSTS functional[52] that has been suggested to exhibit better SCF convergence than the original functional. Note that for τ-dependent functionals we generally include in particular the CDFT versions (using τ_D) that we will denote with a prefix "c".

Computations with the ORCA program contribute additional results for MP2[130] as well as for the double hybrids (DHs, rung 5) B2PLYP[131] and DSD-PBEP86[55,56] (these data are collected in Supporting Information). In general, we will not present data for all functionals at length in the main text but will largely concentrate on statistical analyses for the better-performing functionals. Full shifts and shielding results for all functionals and complexes are given in Tables S17 – S29 and S43 – S55 in Supporting Information, and further statistical data can be found in Tables S30 – S42.

Statistical analyses have been carried out relative to the experimental chemical shifts (as reported in Table S1), using standard deviation (SD), mean signed error (MSE) and mean absolute error (MAE) in ppm, as well as the slope of the linear regression when using the Y-intercept method. To be able to compare performances across different nuclei, we will additionally use dimensionless percentage (relative) deviations normalized to the experimental shift range covered for a given nucleus. Adding these relative statistical measures up (including the slopes), weighted by the number of values for a given nucleus, provides us also with final aggregate relative deviations for the entire test set (aggregate relative SD, aggregate relative MSE, aggregate relative MAE, aggregate slope) for all complexes ("all"). A direct linear regression of shifts across the entire test is of course also possible but would be dominated by the nucleus with the largest shift range, ^{59}Co, and thus be less informative. We furthermore will use histogram plots of relative deviations to trace the origins of the largest deviations for a given method, and we also provide maximum relative absolute errors for each method and nucleus (Figure S4 in Supporting Infromation).

4 Results

A comparison of the structures obtained at BP86-D3(BJ) and TPSSh-D3(BJ) levels. In the following, we will largely focus on the results obtained with BP86-D3(BJ) structures to maintain consistency with previous publications. However, different input structures are known to result in (partly large) deviations in the final shifts (see e.g., Ref. 90). For a subset of functionals we therefore also computed shifts using TPSSh-D3(BJ) structures, which have been found to agree somewhat better with experimental structures.[132] The results are provided in Supporting Information, where statistical comparisons are in Figure S1, while the full numerical data are in Tables S2 – S6.

The relative performance of the functionals in the NMR calculations is essentially the same for both sets of input structures (Figure S1). However, the use of moderate exact-exchange admixture (10%) in the optimizations tends to overall improve agreement with experimental shifts, particularly when hybrid functionals, CDFT variants of τ-dependent functionals or highly parameterized functionals are used for the shielding calculations. That is, the performance of most GGAs and mGGAs is affected insignificantly, with the changes in statistical data mostly below 0.3%. Two exceptions here are cM06-L and cVSXC where the differences between the two structure sets are larger but still below 1.0% in relative deviations. Relative SDs and MAEs are reduced somewhat when using the TPSSh structures. Somewhat larger differences are found for rung 4 functionals. In case of GHs the differences between the two sets increase with exact-exchange admixture: that is, for cTPSSh deviations are still below 0.3% in SD and MAE, for B3LYP they are ca. 1.2%/0.9%, for cPW6B95 1.8%/1.4%, for BHLYP 3.7%/3.2% (reducing the rel. SD from 20.4% to 16.7% and the rel. MAE from 18.7% to 15.5%). Differences for RSHs and LHs are below 2%. That is, while individual shift values may change significantly with input structure, the overall statistical significance is more limited. We can thus in the following concentrate on the BP86-D3(BJ) structures with

some confidence, keeping in mind that the TPSSh-D3(BJ) structures may give overall somewhat improved statistical agreement with experiment. We note additionally that while TPSSh was the top-performer in a systematic evaluation of the structures of 3d-complexes, BP86 was not far behind.[132]

Choice of reference standards. We have evaluated different choices of reference standards, as these can affect statistical evaluations for transition-metal nuclei substantially.[17,18] One set of evaluations, for which we provide statistical data in Tables S14 – S16 in Supporting Information, uses shifts relative to the following reference standards for the different 3d nuclei: $TiCl_4$ ($\delta_{ref.exp.} = 0$ ppm), $VOCl_3$ ($\delta_{ref.exp.} = 0$ ppm), CrO_2F_2 ($\delta_{ref.exp.} = -87$ ppm), $MnCp(C_6H_6)$ ($\delta_{ref.exp.} = -180$ ppm), $Fe(CO)_5$ ($\delta_{ref.exp.} = 0$ ppm), $Co(CO)_4H$ ($\delta_{ref.exp.} = -3721$ ppm), and $Ni(PMe_3)_4$ ($\delta_{ref.exp.} = 40$ ppm). Some of these compounds differ from the usual standards used in the NMR experiments and were chosen because they are either neutral molecules (where the experimental standards are ions) or easier to calculate from an electronic-structure point of view. In these cases, the chemical shifts were converted back to the usual scales using the experimental chemical shifts of the chosen reference compounds. We finally decided, however, to follow earlier precedent for transition-metal nucleus shifts and will focus our main discussion on the Y-intercept method, based on the linear regression of computed shielding constants at a given level against the experimental shift data. The intercept on the Y-axis of this linear fit provides a new reference shift at the given level. The relative performances of different XC functionals are affected only weakly by this choice, also for additional choices of reference standards (even when using "more difficult" reference complexes[17]). The Y-intercept method gives overall the smallest statistical deviations, as it produces a "best linear fit" of the computed shieldings to the experimental shift data for any given method. We assume this to provide the smallest bias. This choice also provides us with slopes of the linear-regression lines as a measure of how well a given method reproduces overall the experimental spread of shifts. We implicitly accept the known disadvantage of this approach: in principle, the chemical shifts need to be re-evaluated each time a new compound is added to the test set. For the current sizeable (and chemically diverse) test sets, we feel that the Y-intercept method provides us with the best measure of the relative performances of different XC functionals.

Artifacts of using τ_{MS}. The τ_{MS} scheme (eq. 1) for rendering the local kinetic energy gauge-invariant is still the most widely used approach to shielding computations with τ-dependent XC functionals. As we had reported,[43,44] we found the scheme to give unphysical paramagnetic contributions for atoms and for the parallel shielding tensor component in linear molecules. While these artifacts clearly also extend to general molecules, the replacement of τ_{MS} by the better founded τ_D (eq. 3) did by no means generally improve the agreement with benchmark data for main-group shieldings. In fact, the previously observed excellent performance of the M06-L meta-GGA, obtained with τ_{MS}, clearly deteriorated with τ_D for the initially studied small main-group shielding test set studied.[43] While the differences were in fact less pronounced for the much larger and diverse main-group benchmark set of Ref. 34, τ_{MS} still gave somewhat smaller MAEs and less negative MSEs. Similar observations held for the VSXC meta-GGA, while matters were dramatically reversed for MN15-L, with much closer agreement with reference data provided within the τ_D framework (with a reduced positive MSE), and τ_D also gave somewhat better agreement with the benchmark data for B97M-V.[34] Small effects on the overall statistics were found for some other meta-GGAs like TPSS, effects for τ-dependent GHs varied. On the other hand, results with several τ-dependent LHs were clearly improved for proton shieldings and for some other situations considered in Refs. 34,43,44.

We will discuss the situation for the molecular 3d complexes of the present study further below and find a number of substantial differences for the relative performance of different schemes compared to the main-group case. In this subsection we want to only show for some spherical atoms and ions with d^{10} configuration that the same artifacts exist for transition-metal nuclei, that they can be even much larger in terms of their shift contributions, and that they are completely eliminated when using τ_D. Table 1 shows total shieldings and paramagnetic contributions for Fe^{2-}, Co^-, Ni, and Cu^+ with τ_{MS} and τ_D for a series of τ-dependent functionals compared to CCSD(T) data. Throughout this analysis, we enforce iso-electronic diamagnetic ($[Ar]3d^{10}$) configurations for all four atomic systems, irrespective of the actual ground state (for Fe^{2-} the CCSD(T) computations produced a symmetry-broken solution only, and the diamagnetic state could not be converged). τ_{MS} gives generally artificial σ^p contributions for all four systems, but the magnitude varies substantially with the overall charge and with the XC functional. The contributions are by far largest for Fe^{2-} and decrease substantially towards Cu^+. We may attribute this trend to particularly small energy denominators and low-lying virtual orbitals for the anionic systems.

In agreement with observations for main-group systems,[43,44] the artifacts of the τ_{MS} scheme are by far smallest (with positive sign) for TPSS and TPSSh. SCAN also gives relatively small artifacts, as do B97M-V, PW6B95, and LH20t (except for Fe^{2-}), with varying signs. For LH20t we note the calibrated exchange-energy densities involved, which appear to reduce such artefacts compared to "uncalibrated" LHs.[44] While M06-L exhibited rather large effects in the main-group case,[43] it occupies an intermediate position for the present 3d systems, together with ωB97M-V and LH12ct-SsifPW92. Particularly large artifacts are seen for VSXC, M06 and, most notably, M06-2X. In some of these latter cases, the paramagnetic artifacts for Fe^{2-} dominate the overall shielding. Fe^{2-} and Co^- may be unrealistic examples, however. The case of the Ni atom may be the best glimpse into the magnitude of these artifacts in a realistic situation, as all Ni complexes studied here have a formal Ni(0) oxidation state (see below). Even here the artifacts are substantial with many of the functionals evaluated. This suggests that the τ_{MS} scheme should be viewed with caution for the 3d nuclei studied here. Calculations with τ_D eliminate the artifacts completely. Now the overall shieldings are exclusively due to the diamagnetic term, and they match the CCSD(T) reference data excellently. We will see below that the fact that τ_D includes also current dependencies for τ in a physically reasonable way becomes an additional asset for the molecular transition-metal complexes studied here.

General statistical evaluation of 3d-nucleus NMR chemical shifts. We start with a bird-eye's view on the statistical evaluation, focussing first on the relative deviations for the weighted average over all 70 complexes, consisting of $12 \times {}^{49}$Ti, $10 \times {}^{51}$V, $10 \times {}^{53}$Cr, $11 \times {}^{55}$Mn, $9 \times {}^{57}$Fe, $9 \times {}^{59}$Co, and $9 \times {}^{61}$Ni shifts. The relative statistical data for the individual nuclei and the combined weighted values are shown in Figure 1, using the Y-intercept method for each

Table 1: Shielding constants and paramagnetic contributions for iso-electronic atomic systems with closed-shell d^{10} configuration (with pcSseg-3 basis).[a]

			CCSD(T)	TPSS	M06-L	VSXC	B97M-V	SCAN	TPSSh	M06	PW6B95	M06-2X	ωB97M-V	12sif[b]	LH20t
τ_{MS}	Fe^{2-}	σ	n.c.[c]	2075.7	1912.9	829.2	1863.1	2112.1	2076.6	946.6	1733.5	-2549.5	1439.5	2172.8	1925.6
		σ^p		10.6	-152.2	-1237.7	-202.0	46.3	11.3	-1118.7	-332.8	-4616.6	-626.0	107.9	-140.2
	Co^-	σ	2175.5	2197.1	2090.5	1856.1	2153.2	2150.2	2195.8	1722.2	2136.6	1757.1	1888.0	2300.8	2165.7
		σ^p	0.0	21.3	-85.2	-321.2	-22.4	-26.2	19.8	-453.5	-40.5	-420.4	-288.0	125.1	-10.8
	Ni	σ	2288.4	2297.1	2180.2	2455.6	2306.0	2282.6	2296.3	2133.8	2286.7	2196.1	2166.9	2377.7	2295.5
		σ^p	0.0	10.1	-107.0	166.6	19.1	-5.0	9.1	-153.3	-1.7	-92.8	-120.2	90.9	7.9
	Cu^+	σ	2397.5	2409.3	2359.3	2516.0	2418.8	2414.5	2408.5	2336.5	2399.7	2360.2	2347.8	2453.9	2404.7
		σ^p	0.0	11.8	-38.6	116.2	21.2	16.3	10.8	-61.3	0.9	-39.2	-49.8	56.6	6.7
τ_D	Fe^{2-}	σ	n.c.[c]	2065.1	2065.1	2066.8	2065.2	2065.8	2065.3	2065.3	2066.3	2067.1	2065.5	2065.0	2065.8
		σ^p		0.0	0.0	0.0	0.0	0.0	0.0	0.0	0.0	0.0	0.0	0.0	0.0
	Co^-	σ	2175.5	2175.7	2175.8	2177.3	2175.7	2176.4	2175.9	2175.7	2177.2	2177.5	2176.0	2175.7	2176.5
		σ^p	0.0	0.0	0.0	0.0	0.0	0.0	0.0	0.0	0.0	0.0	0.0	0.0	0.0
	Ni	σ	2288.4	2287.0	2287.2	2289.0	2286.9	2287.6	2287.2	2287.2	2288.4	2288.9	2287.1	2286.9	2287.6
		σ^p	0.0	0.0	0.0	0.0	0.0	0.0	0.0	0.0	0.0	0.0	0.0	0.0	0.0
	Cu^+	σ	2397.5	2397.5	2397.9	2399.8	2397.6	2398.2	2397.7	2397.8	2398.8	2399.4	2397.6	2397.3	2398.0
		σ^p	0.0	0.0	0.0	0.0	0.0	0.0	0.0	0.0	0.0	0.0	0.0	0.0	0.0

[a] Grey font indicates cases where the converged closed-shell d^{10} configuration exhibits a negative HOMO-LUMO gap.
[b] Abbreviation for LH12ct-SsifPW92.
[c] No convergence to a diamagnetic solution achieved.

nucleus. In this graphic we include only methods where relative MAEs below 18%, relative MSEs between -13% and +13%, relative SDs below 20%, and slopes between 0.4 and 1.4 are achieved for all nuclei. Statistical evaluations for all methods by the Y-intercept method can be found in Tables S30 – S42 in Supporting Information, data for the alternative referencing scheme (see above) are in Tables S14 – S16, while Tables S17 – S29 provide full numerical shift and Tables S43 – S55 the corresponding shielding data. As differences between BP86-D3(BJ) and TPSSh-D3(BJ) structures for the shielding results are insignificant for the overall statistical comparison of the different methods (see above), we focus exclusively on the former set of structures. For τ-dependent functionals we will focus on the better justified τ_D model only (using prefixes "c" as is common for the CDFT treatment) and postpone a discussion of the treatment of τ to a later section. We note already, however, that τ_D provides generally the best agreement with experiment, sometimes dramatically so, except for MN15-L (see below).

We first discuss the aggregate weighted relative MAEs for the different categories of XC functionals (Figure 1, top right). For orientation we note that for the large main-group absolute shielding benchmark of Ref. 34 based on CCSD(T)/pcSseg-3 data, several functionals achieved combined rel. MAEs below 2%, 0.9% in case of the overall best-performing DH DSD-PBEP86 (1.1% for MP2), 1.5% in case of the currently best rung 4 (cLH12ct-SsifPW92) and rung 3 (cB97M-V) functionals. Even a few more functionals made the 1.5% threshold when going to relative shifts.[34] For the present 3d shift evaluations, the best functionals are generally still above 4% aggregate rel. MAE, indicating a generally more challenging situation. We lump the only LDA on rung 1 (SVWN) with the rung 2 GGAs and find that two of the latter, B97D and HCTH, give relatively low rel. MAEs of 5.6% and 5.3%, respectively. The SVWN LDA and the standard GGAs BLYP, BP86, and PBE perform only somewhat more poorly with rel. MAEs of 6.1-6.4%. Strikingly, the "specialized" KT1-KT3 functionals designed for (main-group) nuclear shieldings give clearly inferior results here (rel. MAEs 7.5-8.8%), in spite of their relatively good overall performance for main-group nuclei.[34] Indeed, even SVWN clearly outperforms these three functionals. This shows that their narrow parameterization does not carry over to the present 3d nuclei, consistent with observations that the good performance of these functionals for light main-group shieldings is essentially based on a compensation between errors in the dia- and paramagnetic contributions.[42]

Turning to the meta-GGA functionals (rung 3), we see widely divergent performance. cMN15-L, which performed very well in the main-group case (see above),[34] has been excluded from Figure 1, as it exceeds the boundaries set (see above), mainly due to its rather poor performance for the critical nuclei ^{55}Mn, ^{57}Fe, and ^{59}Co (Table S32). Its final weighted rel. MAE is 13.2%. On the other hand, cM06-L and cVSXC provide the best performances (but only in their τ_D CDFT versions, see further below), with a final rel. MAE of only 4.0% and 4.3%, respectively. Indeed, these are not only the lowest rel. MAEs for rung 3 but for any functional studied here! This is notable, as it defies the usual expectation that the performances of XC functionals usually improve as one moves up the rungs of Jacob's ladder. In the present case this has to do with clearly detrimental effects of EXX admixture for certain transition-metal systems (in particular for ^{53}Cr shifts, see below), and also with the ability of the CDFT framework to cover for important current contributions (see below). The remaining CDFT meta-GGAs, cTPSS, cτ-HCTH, cB97M-V, and cSCAN exhibit intermediate rel. MAEs between 5.3% and 6.7%, which is in the range of the GGAs discussed above. In fact, the rather reasonable performance of cτ-HCTH is slightly inferior to its GGA analogue HCTH, and the exceptionally good performance of cB97M-V for main-group shieldings[34] carries over only partially to the present 3d shift set (rel. MAE 5.3%).

Proceeding to rung 4, we start with the GHs. Only five out of the nine GHs evaluated here are included in Figure 1. Most of the Minnesota functionals exhibit extremely large deviations (Tables S35 – S37 in Supporting Information), with weighted rel. MAEs of 16.7% (cM06-2X), 18.7% (cM06), and 9.9% (cMN15), still much larger deviations are found with other τ frameworks. Again the by far largest deviations are accumulated for ^{55}Mn, ^{57}Fe, and ^{59}Co. In case of cM06-2X the large deviations for these three nuclei can at least in part be attributed to the very large global EXX admixture (54%), as BHLYP exhibits similar deviations (rel. MAE 18.7%). For cM06 and cMN15, other shortcomings related to the description of electron density response in the core and semi-core regions have to be considered as important factors, as found previously for 3d transition-metal hy-

perfine couplings.[133] B3LYP, cTPSSh, and B97-2 are the best-performing GHs (rel. MAEs 5.0%, 5.5%, 5.7%, respectively), as they perform rather well for the three critical nuclei (they exhibit larger deviations for ^{53}Cr, see below). B3LYP had so far been considered the best functional for the later 3d nuclei,[15–18] and it does indeed belong to the overall best-performing functionals. Nevertheless, its overall rel. MAE is larger than those of cVSXC, cM06-L and comparable to those of several LHs (see below) and even to one GGA (HCTH). cPW6B95 (6.2%), and PBE0 (6.8%) follow as intermediate performers among the GHs. We included four RSHs on rung 4, even though previous experience did not suggest them to have any notable advantages over GHs for nuclear shieldings. This is borne out by the results for CAM-B3LYP (6.5%), ωB97X-D (6.7%), ωB97X-V (6.8%), and cωB97M-V (6.2%), which are comparable to, e.g., cPW6B95 or PBE0. For cωB97M-V, the CDFT variant actually deteriorates the results very slightly in comparison to the other τ models.

This brings us to the LHs, where position-dependent EXX admixture indeed has been considered and previously found to be[34,43,44] an advantage for nuclear shieldings in the main-group case. While cLH12ct-SsifPW92 and cLH12ct-SsirPW92 had been found to perform best overall for non-hydrogen main-group nuclei in these studies (followed by cLH20t, which performs better for proton shieldings), in the present case LHs with a smaller prefactor of the t-LMF and thus lower overall EXX admixtures perform better. That is, cLH14t-calPBE (4.9%) and cLH07t-SVWN (5.1%) show the overall lowest rel. MAEs, together with cmPSTS that features a more complicated LMF (5.2%). These values are comparable to those for B3LYP and HCTH but remain somewhat above those of the best-performing cVSXC and cM06-L (see above), attributable to the ^{53}Cr values (see below). Interestingly, LH07s-SVWN with an s-LMF based on the reduced density gradient is not far behind here (5.3%), followed by the general-purpose cLH20t (5.6%). The larger deviations for cLH12ct-SsifPW92 (7.7%) and cLH12ct-SsirPW92 (6.7%) are due to larger deviations for several nuclei and related to the large EXX admixture. cLHJ14 (6.0%) based on correlation length is intermediate among the LHs.

The current representatives of rung 5 on the ladder, the B2PLYP and DSD-PBEP86 DHs, are not at all suitable for the 3d-nucleus shifts studied here (see Table S29 in Supporting Information). As expected, their combination of large constant EXX admixtures and MP2 correlation make them largely useless for transition-metal shifts, in contrast to the clearly best performance over all functionals in the main-group case by DSD-PBEP86.[32,34] The DHs and MP2, as well as the underlying HF method, are not included in Figure 1, as they exceed the set boundaries by far for all nuclei except for ^{49}Ti. As HF is a very poor starting point, MP2 fails completely as well, and this failure is only partly corrected in the DHs (somewhat better with B2PLYP than with DSD-PBEP86, which has a larger EXX admixture of 70%).

Based mainly on the aggregated rel. MAE values the overall top-performing functionals for the entire set are cM06-L, cVSXC, cLH14t-calPBE, and B3LYP (with values up to 5%), closely followed by LH07t-SVWN, LH07s-SVWN, cmPSTS, HCTH, cB97M-V, cTPSSh, and LH20t (with values up to 5.6%). A closer understanding of what drives these overall trends requires looking at the individual nuclei, as we will do below. This will also involve the rel. MSEs (Figure 1, bottom left) and the slopes of the regression lines (Figure 1, bottom right). The aggregates of these two quantities are less informative, and particularly the slopes are of more interest when analyzed for the individual nuclei (see below). We note only here that the aggregate rel. MSEs are small and negative (by not more than -2% for semi-local functionals, a bit more when EXX admixture is present), and they arise from a compensation between positive and negative values for different nuclei (see below). The widths of the distributions of errors are indicated by the rel. SDs (Figure 1, top left). These give largely the same order of functionals as the rel. MAEs.

A closer look at the most critical nuclei, ^{55}Mn, ^{57}Fe, and ^{59}Co. These nuclei, as well as ^{61}Ni discussed below, are the best-known examples for the advantage of GHs with moderate EXX admixture such as B3LYP over simple GGAs,[15–18] while GGAs gave better agreement with experiment for earlier 3d nuclei like ^{53}Cr and some earlier 4d nuclei.[25–27,134] We have mentioned in the introduction some of the arguments put forward to explain these observations. Yet we find these three later 3d nuclei to also dominate the aggregated relative deviations discussed in the previous subsection, at least for those functionals that do not make it into the top group. It seems thus important to have a closer look at these critical nuclei, focussing again on the better-performing functionals. Starting again with the rung 1-2 functionals, we see that indeed ^{55}Mn and ^{57}Fe account for the largest rel. MAEs, on the order of 9-12% for the simpler functionals (SVWN, BLYP, PBE, B97D, HCTH), and to 13-17% for the "specialized" KT1-KT3. For ^{59}Co, the rel. MAEs are lower, about 5-8% for the simple LDA/GGA functionals, 11-13% for KT1-KT3. It is notable, that the rel. MSEs often reach substantial fractions of these values, with a positive sign for ^{55}Mn but with a negative sign for ^{57}Fe and ^{59}Co. These opposite signs seem to generally contribute to the overall relatively small negative aggregate rel. MSEs that we discussed above. The relatively good performance of HCTH and B97D among the GGAs is reflected in relatively low deviations for these nuclei and is consistent with earlier findings on a smaller set of TM complexes.[135] Note also that the GGAs all give too small slopes of the regression lines for these three nuclei.

While several CDFT meta-GGAs give similar (cτ-HCTH, cTPSSh) or much larger (cMN15-L) deviations for the same nuclei, the top-performing cM06-L and cVSXC are clear outliers and improve the MAEs and MSEs, giving rel. MAEs of 3.9-6.0% (but only in their CDFT implementations), comparable to the less critical nuclei (see below), and with slopes close to 1.0. This is indeed the reason for their overall top performance. Notably, these two functionals also give very small rel. MSEs (and low SDs). In contrast, the very poor performance of cMN15-L for the overall test set is closely linked to its large deviations for these three nuclei. cB97M-V performs only somewhat inferior (rel. MAEs 5.4-7.3%) to the top-performing cM06-L and cVSXC.

The better-performing GHs in the general overview above, such as B3LYP, cTPSSh or B97-2, also reduce the deviations most notably for these three nuclei (to 3.7-7.8% rel. MAE, 8.9% for ^{55}Mn in case of cTPSSh), to the extent that the rel. MAEs of other nuclei are typically larger (see below). The slopes are again close to 1.0 (up to 1.19 with B97-2 for ^{59}Co) for these three functionals. cPW6B95 also has fairly low rel. MAEs for these three nuclei (4.5-8.1%), PBE0 and three of the RSHs also remain generally below 10%. All other GHs (BHLYP, cM06, cMN15, cM06-2X) exhibit much larger de-

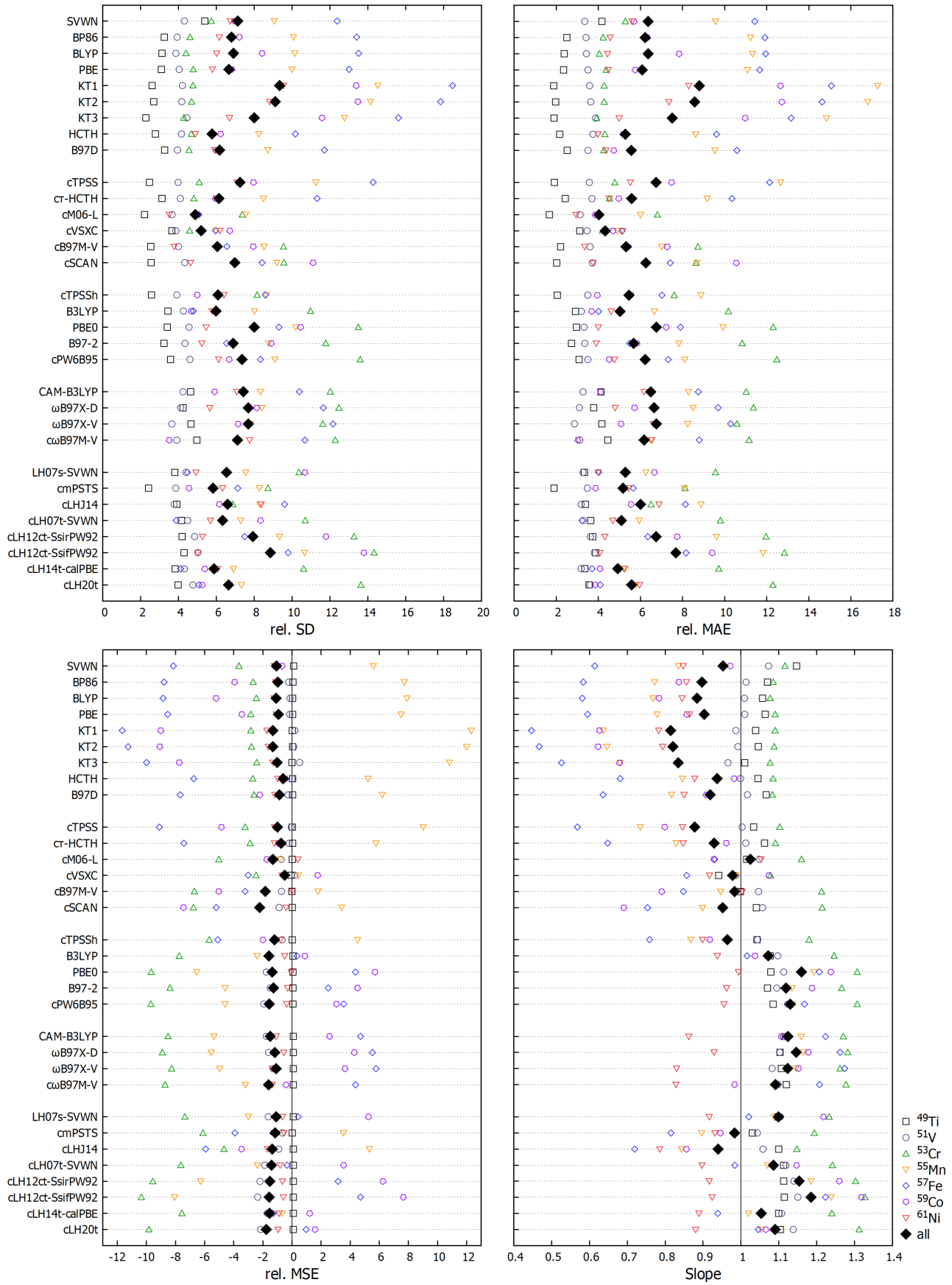

Figure 1: Relative standard deviations, mean signed errors, mean absolute errors in %, as well as slopes of the linear regression for the individual nuclei (hollow symbols) and their weighted aggregate (filled black symbols) for various XC functionals (using τ_D for τ-dependent functionals).

viations, including dramatically overestimated slopes. Even larger deviations are seen for HF, MP2 and the DHs, largely indicating erratic behavior.

Among the best-performing LHs, cLH14t-calPBE, cLH07t-SVWN, and cLH20t all have rel. MAEs below 6% for these three nuclei, comparable to cM06-L or cVSXC. LH07s-SVWN, cmPSTS, cLHJ14, cLH12ct-SsifPW92, and cLH12ct-SsifPW92 give slightly larger values. For all of these LHs, as well as for cM06-L, cVSXC, B3LYP, indeed for most hybrids, the largest rel. MAEs are now contributed by other nuclei (see below). Indeed, we can define the best-performing functionals as those where this is the case, i.e. where the deviations for the most critical nuclei ^{55}Mn, ^{57}Fe, and ^{59}Co have been reduced below those for some seemingly less demanding ones. When taking a weighted average of the rel. MAEs for just these challenging three later 3d nuclei, we find six functionals competing closely with values below 5%, in the order cLH14t-calPBE < cLH20t = cM06-L < cLH07t-SVWN < cVSXC < B3LYP. It is notable that this includes three LHs, the B3LYP GH, but also two CDFT meta-GGAs.

The spread of shifts, the slope of the regression lines, the scatter, as well as the dependence on the electronic-structure method for a given nucleus is typically dominated by the systems with the largest paramagnetic (de-)shielding contributions. This holds even more so for transition-metal complexes where the incomplete metal d-shells give rise to large paratropic currents around a given metal nucleus. Indeed, our analyses confirm that the performance of a given method for a given subset is governed largely by the complexes with the most negative absolute shielding values, even though small deviations from this notion can be found. The Y-intercept method tends to hide somewhat these effects, as the reference shift value is adapted for a given method. Other choices of reference values may also be misleading. Therefore it is best to examine the absolute shielding values provided in Tables S43 – S55 in Supporting Information for better understanding.

The subset for the prototypical late 3d nucleus ^{57}Fe consists exclusively of organometallic systems, which typically are considered to provide strong ligand fields. Nevertheless, considerable paramagnetic contributions are found, for example in case of Cp ligands. The rel. MSE and the slope of the linear regression are largely dominated by [$FeCp_2$], followed by [$FeCp(CO)_2iPr$] and [$FeCp(CO)_2Me$]. [$Fe(CO)_3(CH_2CHCHO)$] exhibits the second largest shift after [$FeCp_2$] but has a smaller dependence on the functional than the three Cp complexes, potentially due to the lack of support for delocalized currents by a Cp ligand. While functionals that enhance paramagnetic contributions by a) EXX admixture or b) CDFT τ contributions also lead to more deshielding for the remaining complexes, they do so to a lesser extent. This explains the effects on slope and MSE. Indeed, [$FeCp_2$] has been chosen earlier for closer analysis of the effects of EXX admixture for this very reason,[24] and we have already mentioned the rationalizations, i.e. energy gaps and CPKS coupling terms on one hand, and delocalization errors on metal-ligand covalency reducing the PSO matrix elements on the other hand. Just as an example, the computed absolute shielding constants for [$FeCp_2$] grow more negative with increasing EXX admixture in the series BLYP, B3LYP, and BHLYP as -2747.3 ppm > -4518.8 ppm > -9395.9 ppm. Combined with similar trends for the two further Cp complexes and much smaller changes for the less deshielded systems, this controls MSEs and slopes, with the middle value for B3LYP giving the best representation. Similarly, cM06-L gives a shielding value of -4057.2 ppm, while its non-CDFT variants give much less deshielded values in the range -2300 ppm to -2600 ppm, similar to simple GGAs (similar but less dramatic effects of τ_D are found for VSXC). We can thus conclude that current-dependencies of the response functionals are of major importance here, be it via EXX admixture or via the CDFT treatment of τ.

The ^{59}Co subset is represented by complexes with a much more diverse range of electronic structures and ligand types, and it exhibits the by far largest shift range of any of the nuclei studied here. This has made ^{59}Co NMR such an important subfield. The most deshielded values are found for classical Werner-type ligands with a relatively weak ligand field, which give rise to small ligand-field splittings and consequently low-lying excited states. The complexes dominating the MSEs and slopes are $[Co(H_2O)_6]^{3+}$, $[Co(acac)_3]$, $[Co(NH_3)_4(CO_3)]^+$ and $[Co(NH_3)_6]^{3+}$. As described above for the iron complexes, these systems exhibit the largest dependencies on the functional, and for example both EXX admixture and CDFT τ contributions in the two mentioned CDFT meta-GGAs provide more negative shieldings (larger shifts). The least deshielded values and thus smallest dependencies on the functionals are represented by the carbonyl complexes $[Co(CO)_4H]$ and $[Co(CO)_4]^-$. That is, in spite of the rather more diverse electronic-structure characteristics of the Co complexes, the mechanisms that determine the dependencies on the functional are comparable as for the Fe systems discussed above. Recall that some of the charged species from this subset also exhibit the largest solvent effects on the shifts, reducing the largest values to some extent, but they are not considered in this comparison of functionals (cf. Computational Details above, as well as Table S7 and Figure S2 in Supporting Information).

A somewhat mixed situation pertains to the ^{55}Mn subset, where the most deshielded values represent both high ($[MnO_4]^-$) and lower ([$MnCp(C_7H_8)$], [$MnCp(C_6H_6)$]) oxidation states. It appears that similar effects of extended paratropic currents as discussed above for [$FeCp_2$] are relevant for the two Cp complexes. In contrast, the permanganate ion represents high-oxidation-state situations with d^0 configuration that are also of importance for the earlier 3d elements, e.g. for ^{53}Cr (see below). Nevertheless, both EXX admixture and CDFT τ contributions lead to more deshielded values for both types of systems. The less deshielded end with smaller dependences on the functional is in this case represented by several carbonyl complexes. The dominance of the most deshielded systems can again be exemplified by the slopes of the regression lines as a function of EXX admixture. For the entire subset they increase overall steeply, e.g. as 0.77 (BLYP), 1.07 (B3LYP), 1.77 (BHLYP). Removing the three most critical complexes alters this substantially to 0.61 (BLYP), 0.81 (B3LYP), 1.07 (BHLYP). Now the larger EXX admixture of BHLYP might even seem more favorable. This makes even more obvious that part of the challenge of these later 3d nuclei indeed arises from some complexes with extremely large paramagnetic shielding contributions. Clearly, the best-performing functionals also benefit from some error compensation. Nevertheless, standard GGA functionals tend to underestimate the paramagnetic contributions for these three subsets systematically, and this can be cured partly by moderate (constant or position-dependent) EXX admixture or CDFT τ contributions. The latter can be exemplified by the shielding value for [$MnCp(C_7H_8)$], which is -5392.5 ppm for cM06-

L (only somewhat less negative than the B3LYP value of -5814.6 ppm, comparable to the cLH14t-calPBE value of -5268.7 ppm), while it is in the range -3300 ppm to -3600 ppm for the non-CDFT variants of this functional. Similar trends hold for $[MnO_4]^-$) or $[MnCp(C_6H_6)]$.

Note also, that some of the most deshielded systems for these three nuclei do already exhibit substantial triplet instabilities when larger EXX admixtures are used, as with BHLYP. This pertains, e.g., to $[FeCp_2]$, $[Co(H_2O)_6]^{3+}$, and $[MnCp(C_7H_8)]$ (the same holds for $[Mn(NO)_3(CO)]$). This will be a larger issue for the discussion of the ^{53}Cr subset (see below).

Examination of results for ^{61}Ni, which is represented by electronically less diverse complexes. The reason for a somewhat diminished diversity of electronic structures for the ^{61}Ni complexes is, that all of the experimentally measured ones correspond to the Ni(0) formal oxidation state and a relatively symmetrical coordination environment. The likely origin for this limitation appears to be the large electric quadrupole moment of ^{61}Ni,[136] when combined with large electric field gradients of the common square-planar Ni(+II) complexes, as well as a low natural abundance.[3] This leads probably to very broad lines, rendering experimental observation very difficult.

^{61}Ni is another nucleus for which the initial computational evaluation by one of us had suggested the B3LYP GH to outperform the BPW91 GGA as well as the BHLYP GH with higher global EXX admixture.[18] The GGA was found to underestimate somewhat the spread of shifts, while BHLYP gave larger scatter. The present broader evaluation confirms this to some extent but provides further insights. We start by noting that most semi-local functionals exhibit small negative rel. MSEs between -1.7% and -1.1% and too low slopes, between 0.78 and 0.88. Exceptions are again caused by several CDFT meta-GGAs, such as cM06-L (rel. MSE +0.4%, slope 1.05), cMN15-L (rel. MSE +0.1%, slope 1.02), cVSXC (rel. MSE -0.7%, slope 0.92), cSCAN (rel. MSE -0.4%, slope 0.95), and cB97M-V (rel. MSE +0.0%, slope 1.00). This leads to an improvement of the rel. MAEs from about 4-6% for the simpler GGAs and LDA and up to 8% for KT1 and KT2 to only 2.9% for cM06-L, and 3.3%–3.7% for cB97M-V, cMN15-L and cSCAN (cVSCX lags somewhat behind, 5.2%). Obviously, the underestimate of the slope by semi-local functionals is much less pronounced here than for the above three critical nuclei, likely due to the narrow range of electronic structures of the Ni(0) complexes, and due to the resulting overall smaller shielding range of less than 2000 ppm. The most deshielded values arise from $[Ni(cod)_2]$, $[Ni{-}t,t,t{-}cdt(PMe_3)]$ and $[Ni{-}t,t,t{-}cdt(CO)]$, the most shielded one from $[Ni(C_2H_4)_2PMe_3]$. EXX admixture does improve the spread moderately. Here even somewhat larger admixture is tolerated in the GHs (e.g. slope 0.94 for B3LYP, 0.96 for B97-2, 0.99 for PBE0, 1.03 for BHLYP), and most GHs, RSHs or LHs give slopes that are still below unity. Indeed, now the LHs that performed best for the non-hydrogen main-group shieldings, cLH12ct-SsifPW92 and cLH12ct-SsifPW92, are competitive as well, but still inferior to cM06-L. CDFT τ contributions for the latter functional (somewhat less so for cVSXC) have similarly moderate effects that increase the slope and improve the MSEs.

Overall the picture is less clear-cut than for some of the other nuclei, as most semi-local functionals and even hybrids with moderate EXX admixtures give somewhat too small slopes, but many of these functionals still have reasonably low rel. MAEs and small negative rel. MSEs for ^{61}Ni. The poorer performances of cM06-2X and cMN15 should be mentioned, as should the again very poor performances of HF, MP2, and the DHs (see full shift results in Tables S23, S24 and S29, and statistical data in Tables S36, S37 and S42 in Supporting Information). Triplet instabilities play a minor role here. Except for Hartree-Fock, MP2, and DSD-PBEP86, where several Ni complexes feature instabilities, only $[Ni(cod)_2]$ seems to be sensitive for functionals with large EXX admixtures like BHLYP or M06-2X.

Results for ^{53}Cr and the issue of triplet instabilities. ^{53}Cr is the 3d nucleus where EXX admixture most clearly has been found to be detrimental in a past study, with B3LYP giving a too large spread of values as well as more scatter than the BPW91 GGA.[27] We note that the complexes for which data are available fall into the two categories of very low (0) and very high (+VI) oxidation states. In agreement with the earlier work, we find LDA and all GGAs to give comparably small rel. MAEs on the order of ca. 4-5% (5.3% for SVWN), with small negative rel. MSEs between -2.4% and -3.6%. This suggests that the reasons that render EXX admixture important for the aforementioned nuclei do not apply here to the same extent. As we move to the CDFT versions of the meta-GGAs, this picture is modified somewhat, in an interesting way: now the overall top-performing cM06-L (6.8%) actually gives larger rel. MAEs than its otherwise inferior counterparts cTPSS (4.8%) or cτ-HCTH (4.5%). cB97M-V, cSCAN and cMN15-L give rel. MAE of 8.7%, 8.6%, and 12.3%, respectively, in this case clearly poorer than their non-CDFT variants (see Tables S32 and S33, as well as discussion below). But cVSXC still performs excellently (rel. MAE 4.2%, rel. MSE -2.5%) in this case.

We clearly confirm the notion that Hartree-Fock exchange is detrimental for the treatment of the ^{53}Cr shifts: all GHs exhibit larger rel. MAEs than the GGAs, increasingly so with growing EXX admixture. That is, cTPSSh (7.6%) performs worse than its underlying cTPSS meta-GGA but better than B3LYP (10.2%), B97-2 (10.8%), PBE0 (12.3%), cM06 (11.5%), or cPW6B95 (12.5%). GHs with larger EXX admixtures, such as BHLYP or cM06-2X, perform even much worse here, with the notable exception of cMN15, which is comparable to B3LYP in this case (rel. MAE 10.1%, but only in its CDFT variant), in spite of a larger global EXX admixture of 44%. The RSHs perform comparably as the PBE0 or cM06 GHs in this case. The detrimental effect of Hartree-Fock exchange is particularly apparent in the HF calculation, which fails completely here and gives larger deviations than for any of the other nuclei (see Table S29 for shifts vs experimental data and Table S42 for statistical data). Consequently, MP2 or the DHs also fail completely for ^{53}Cr. Notably, the HF calculations give dramatically negative MSEs, and this carries over in reduced form to negative rel. MSEs for all (global, range-separated or local) hybrid functionals. In contrast, MP2 exhibits catastrophically positive rel. MSEs, which carries over to the DHs. From the viewpoint of the spread of values, all semi-local functionals already have slopes above one, and this is aggravated by EXX admixture.

Closer analysis has to again focus on the absolute shieldings, as the Y-intercept-based shifts cloud which systems actually cause the overall largest variations, given that the reference value also changes from method to method. The most deshielded values and the largest variations with the functional arise clearly from the six Cr(+VI) complexes, while the most shielded end is represented by the four Cr(0)

carbonyl complexes. The experimental shifts of these two groups of complexes are separated by approximately 2000 ppm, while the variations within a given group are below 350 ppm. It is thus clear, that the performances of the different functionals are largely controlled by how well they represent the shielding differences between the two groups, and this is largely determined by how well the Cr(+VI) d^0 complexes and their low-lying LMCT-type excited states are described. We may use $[CrO_2Cl_2]$ as a good example for a Cr(+VI) complex with large deshielding and a large dependence on the functional and contrast it with $[Cr(CO)_6]$ on the most shielded side (see Tables S43 – S55). The difference in experimental shifts between these two complexes is 2058 ppm. Already the simplest semi-local functionals give a too large difference of about 2300-2400 ppm, due to a too negative shielding for $[CrO_2Cl_2]$, consistent with an overestimated slope in the range 1.11-1.17, which is slightly more than the corresponding slope of the regression for the entire subset. The difference is further increased by EXX admixture as well as CDFT τ contributions. For example, B3LYP gives a difference between the two shieldings of 2753 ppm, cLH14t-calPBE 2703 ppm, and cM06-L 2517 ppm (compared to 2100-2200 ppm for its non-CDFT variants). The detrimental effect of even small EXX admixtures is thus immediately apparent from just the differences between those two complexes. As the CDFT τ contributions also increase the difference somewhat, they also lead to too large slopes and even more negative MSEs in the final shifts. Indeed, it may well be that the diversity of the ^{53}Cr subset is insufficient to get a more balanced description. This is not easy to correct, however, as any experimental data available fall into either the tetrahedral Cr(+VI) oxo or the octahedral Cr(0) carbonyl category. Less symmetrical complexes pose difficulties for experimental detection due to large electric-field gradients and thus line-broadening for the quadrupolar ^{53}Cr nucleus. For example, Hafner et al. examined a larger series of more than 50 Cr(0) carbonyl and phosphine complexes, most of them (46) with carbene ligands.[137] However, their shifts span a range of less than 300 ppm. Similarly, the range of shifts for experimentally accessible Cr(+VI) oxo complexes is also small so far. Consideration of a larger number of complexes would thus likely not cure the basic problem of the too large relative shifts between Cr(+VI) and Cr(0) complexes.

One may wonder to what extent triplet instabilities are the reason for the unfavorable effect of EXX admixture on the ^{53}Cr shifts. Hartree-Fock exhibits triplet instabilities for *all* chromium complexes studied here, and consequently HF, MP2 and DH shift results are completely erratic. Following Ref. 36, we may consider this as an artificial spin-symmetry breaking, as GHs with lower EXX admixture, such as B3LYP, or LHs and RSHs produce stable spin-restricted solutions. Yet BHLYP is triplet-unstable for the three Cr(+VI) complexes $[CrO_2Cl_2]$, $[CrO_2F_2]$, and $[CrO_3Cl]^-$, i.e. for several of the systems with the largest paramagnetic contributions. It seems possible that "incipient" or "latent" spin-symmetry breaking could be invoked in this context to rationalize the detrimental effects of EXX admixture. While BHLYP also exhibits triplet instabilities for several Mn, Fe, and Co complexes, in those cases the effects seem to be partly compensated due to the more diverse nature of the electronic-structure characteristics making up the given subset of complexes.

The less difficult earlier 3d nuclei ^{51}V and ^{49}Ti. The two early 3d nuclei represent smaller dependences on the XC functional than those discussed so far. Indeed, the ^{49}Ti subset is the only one for which even HF, MP2, and the DHs perform reasonably well (see below).

We start our discussion with the slightly more demanding ^{51}V subset. Here the rel. MAE values for the semi-local functionals range from 3.1% (cM06-L) to 3.9% (KT3), excluding some of the non-CDFT variants, which give poorer results. The relative MSEs for these functionals are small and can be negative or positive, and slopes close to 1.0 are found. The relative MAEs are also between 3.1%–3.8% for all GHs, RSHs, and LHs, except for a few cases, most notably ωB97X-V with a rel. MAE of 2.9%, the top performing functional in this subset. cM06-2X (4.3%), cM06 (5.6%), and BHLYP (5.8%) give clearly larger deviations. Relative MSEs also tend to remain small in many cases except for a few functionals (including some non-CDFT variants of τ-dependent functionals), but they tend to become more consistently negative. Indeed, slopes are now around 1.10 (larger ones are obtained for the less well-performing GHs). Hartree-Fock and particularly MP2 perform nevertheless clearly worse here too, with large negative MSEs, particularly for MP2. Indeed, the majority of vanadium complexes studied here exhibits triplet instabilities at HF level (Table S55). Most of these are cured for the DHs, which perform indeed much better than HF or MP2 while still falling behind most other functionals.

Overall the ^{51}V subset is dominated by V(+V) oxo complexes and VF_5, while the two V(-1) carbonyl complexes bring in additional diversity. It seems, however, that the different ligand types available for the V(+V) complexes improve the balance of the overall set, which may be an advantage over the available ^{53}Cr data discussed above. The largest paramagnetic contributions arise for the model complex $[VOMe_3]$ (and the experimentally studied counterpart $[VO(CH_2SiMe_3)_3]$), as the pure σ-donor methyl ligands leave the system coordinatively unsaturated with low-lying vanadium 3d-type virtual orbitals (additional π-donor ligands like fluoride or chloride help increase the HOMO-LUMO-gap and thus reduce the paramagnetic contributions somewhat). The least deshielded value is represented by $[V(CO)_6]^-$. As discussed in several cases above, EXX admixture and CDFT τ contributions increase the differences between these extreme cases, and the changes for the oxomethyl complex are most important in this context. However, the dependencies are much less pronounced than those discussed so far, and the overall somewhat too large difference for hybrid functionals like B3LYP is in part outweighed by the smaller statistical scatter over the entire subset, giving low rel. MAEs.

Turning finally to the ^{49}Ti shifts, we find this to be the only subset, where Hartree-Fock is not a catastrophical starting point, and where thus also MP2 or the DHs do not deviate much from the other functionals. Incidentally the first calculations of ^{49}Ti chemical shifts had been reported at the IGLO-HF level - in hindsight a serendipitously good choice of target systems for this method.[138] Except for some non-CDFT variants of certain τ-dependent functionals (see Tables S32, S33 and S35 – S38), all functionals have rel. MAEs below 5%, including HF, MP2, and the DHs. Now even the KT1-KT3 functionals perform well with rel. MAEs of around 2%, while cM06-L (1.7%) is the top performer. cTPSSh (2.0%) has the lowest value for a GH, cmPSTS (1.9%) for an LH, while most GHs, RSHs or LHs tend to have somewhat larger rel. MAEs above 3%. These observations are consistent with previous work on a much smaller sample of functionals.[28] A few worse performances of highly

parameterized functionals should also be mentioned, such as cMN15 or cM06, which exhibit a rel. MAE of 5%, while LDA (SVWN) gives 4.2%. Most functionals also give slopes relatively close to one, except for a few (SVWN 1.15, cM06 1.17, cMN15 1.16, MP2 1.15, and some non-CDFT variants of τ-dependent functionals).

A closer look at the role of exact-exchange admixture for error distributions (Figure 2). To provide some further insights into how EXX admixture in GHs and LHs shifts the performances for the different 3d nuclei, in Figure 2 we use rel. SD curves (black solid line) on top of histogram plots of the number of shifts of all subsets in the error ranges from -80% to 140% in 10 % blocks. We compare the series of the closely related BLYP, B3LYP and BHLYP with constant EXX admixtures of 0%, 20%, and 50%, as well as the two cLHs cLH14t-calPBE and cLH20t, which are both based on calibrated exchange-energy densities. They have t-LMF prefactors of 0.500 and 0.715, respectively, and thus also represent different EXX admixtures. The histogram representation allows us to follow how the overall width of the aggregate rel. SD distribution over the entire test set is dominated by certain nuclei. Similar information is provided by max. rel. AEs (see Figure S4 in Supporting Information).

Starting with the BLYP curve, we see its medium width to be caused by positive deviations in the 20% block for ^{55}Mn shifts and a few negative deviations in the -40% and -20% blocks for ^{57}Fe (and ^{59}Co) shifts. This is consistent with the observation that these critical nuclei dominate the errors for most semi-local functionals (with the exception of some CDFT meta-GGAs), with positive MSEs for ^{55}Mn and negative ones for ^{57}Fe. As we move to 20% EXX admixture in B3LYP, the distribution narrows noticeably, larger errors for the three critical nuclei are removed, but now negative deviations in the -30% and -20% blocks occur for ^{53}Cr and ^{55}Mn, consistent with the generally negative MSEs of hybrid functionals for these two nuclei. As we increase the EXX admixture to 50% for BHLYP, the distribution widens dramatically. Now deviations for ^{53}Cr in the -70% and -60% blocks and for ^{55}Mn in the -60% through -20% blocks dominate the negative flank of the curve, while overshooting for ^{57}Fe in the +50%, +60% and even +130% blocks is seen, together with positive deviations for ^{59}Co in the +30% and +60% blocks. It is thus clear that too high constant EXX admixture enhances the negative MSEs for the early nuclei ^{53}Cr and ^{55}Mn, but positive deviations start to appear for ^{57}Fe and ^{59}Co, which are absent for the more moderate EXX admixture of B3LYP. We may trace this potentially to triplet instabilities, in particular for certain ^{53}Cr and ^{55}Mn complexes (see above). We noted already the smaller dependencies of the ^{49}Ti, ^{51}V and ^{61}Ni shifts on the EXX admixture. In consequence, these nuclei do not dominate the widths of the distributions.

Similar observations can be made for the two cLHs: both functionals have relatively narrow distributions and do not differ much on the side of positive deviations (shifts of all nuclei except ^{51}V appear in the +10% block). Similarly to the B3LYP GH, for both LHs the negative flank of the distribution curve is dominated by some ^{53}Cr shifts, to a lesser extent by ^{55}Mn shifts (again except for ^{53}Cr and ^{59}Co all nuclei appear in the -10% block). These deviations increase somewhat with increased t-LMF prefactor for cLH20t (the ^{53}Cr error margins increase from -24% to -30%, compared to -26% for B3LYP), explaining why this functional arrives at a slightly inferior overall performance and a slightly wider distribution of errors compared to cLH14t-calPBE for the entire test set, while being entirely competitive for the later 3d nuclei. We note, however, that the average EXX admixture of LH20t might be compared best to a GH with around 30-35% EXX admixture (as indicated, e.g., by its performance for mixed-valence (de-)localization [50]). In spite of this, its problems caused by triplet instabilities are much less pronounced than for comparable GHs (see above). Yet we also see that the flexibility of position-dependent EXX admixture for the present LHs is not yet sufficient to allow an improvement of the performance for the later 3d nuclei without any deterioration for the earlier ones. This represents a goal for the currently ongoing construction of more sophisticated local mixing functions for LHs.

Figure 3 widens the lens to a larger selection of the better-performing functionals and can correspondingly narrow the scale of the error distributions. Starting with the semi-local functionals, the plots for HCTH and cB97M-V confirm that the widths of the distributions are dominated by positive deviations from ^{55}Mn complexes (and a few ^{59}Co and ^{61}Ni systems) and by both negative and positive deviations from ^{57}Fe and ^{53}Cr complexes (some ^{61}Ni and ^{59}Co systems also appear). The two CDFT meta GGAs cM06-L and cVSXC change the picture decisively in terms of the much smaller magnitude of the deviations for ^{55}Mn, ^{57}Fe and in terms of the nature of the also reduced negative deviations: for cM06-L these are now contributed by some ^{53}Cr, ^{57}Fe and ^{59}Co complexes, and even a few ^{55}Mn systems, and for cVSXC these smaller negative deviations are now also distributed over different nuclei, including ^{53}Cr, ^{57}Fe and ^{61}Ni. The consequence for the latter functional is, that rel. MAEs are below 5.2% for all nuclei, indicating a particularly balanced behavior (see above).

The three GHs cTPSSh, B3LYP, and cPW6B95 can be used to look again at the role of (constant) EXX admixture. As mentioned above, the largest (moderate) negative deviations for B3LYP arise from ^{53}Cr shifts, to a lesser extent from ^{55}Mn. The largest positive deviations come from ^{61}Ni and ^{59}Co, but they reach only into the +10.0 block (ranging from +8.75%–11.25%). In contrast, cTPSSh (10% EXX admixture) is somewhat closer to the semi-local functionals, as its slightly wider distribution is dominated by positive deviations for ^{55}Mn and by a less structured mix of negative deviations that include ^{53}Cr and ^{57}Fe. The larger EXX admixture (28%) of cPW6B95 also widens the error distribution compared to B3LYP but retains the typical origins for hybrids: negative deviations for ^{53}Cr and ^{55}Mn, positive ones for ^{59}Co, ^{57}Fe, ^{61}Ni, now ranging from -30% to +20%. In addition to the already discussed LHs cLH14t-calPBE and cLH20t, Figure 3 also includes cmPSTS and cLHJ14, which are both not based on a t-LMF. The most notable feature of the somewhat wider distribution of cLHJ14 are positive deviations for ^{55}Mn. Interestingly, the negative deviations are covered by some ^{57}Fe, ^{53}Cr, ^{59}Co, and ^{61}Ni shifts, which differs from the typical behavior of most of the hybrid functionals. This results from an overall low EXX admixture for this LH in the core region.[34] cmPSTS, which has a similarly narrow distribution as cLH14t-calPBE, differs from the behavior of the latter by clearly having a larger positive deviation for ^{55}Mn (the rel. MSE of 3.5% for cmPSTS should be compared to -0.7% in cLH14t-calPBE). The largest negative deviations arise from some ^{53}Cr and ^{57}Fe complexes.

The role of current-dependency in the τ-dependent functionals for their overall performance. So far we have concentrated on the CDFT variants of the τ-dependent functionals using the τ_D scheme, but we men-

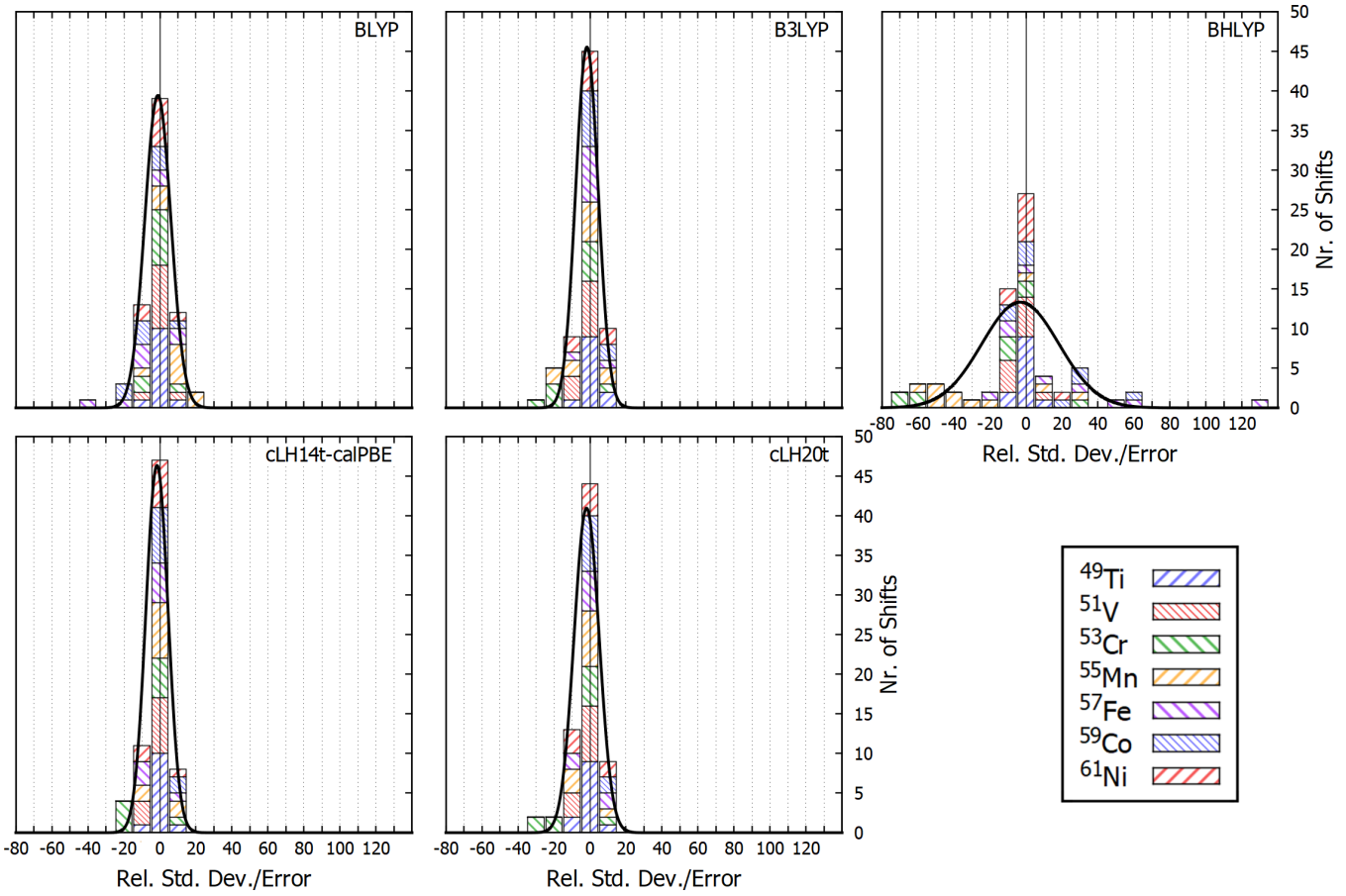

Figure 2: Standard deviation plots (solid black line) on top of histogram deviation plots of the individual 3d transition metal test sets, comparing BLYP to B3LYP and BHLYP (top), and cLH14t-calPBE to cLH20t (bottom) within the range from -60 % to +140 % in blocks of 10 %.

tioned from time to time the non-CDFT variants. As has been discussed previously,[42–44,47–49,60] τ_D is the physically most appropriate way of using these functionals for magnetic properties, as this turns them into proper CDFTs, if only via their τ-dependence. It is difficult to derive meaningful CDFT functionals at LDA or GGA levels, while EXX admixture is of course a way to bring in current contributions to some extent. Indeed, we have argued previously that the position-dependent EXX admixture of LHs is helpful for this purpose.[43,44]

We also showed above and in Refs. 43,44 that the τ_{MS} scheme, while rendering τ gauge invariant, also introduces paramagnetic artifacts that are easy to demonstrate for atoms but are more difficult to identify for general molecules. We can partly disentangle these artifacts from the genuine current contributions by comparing also to two further models to treat τ, a) by using the original gauge-dependent τ (with the gauge origin placed at the center of mass, termed τ_C) and b) by eliminating the gauge dependence in an *ad hoc* way[43] as done in the ORCA code (τ_0). These two models do not generate paramagnetic artifacts for atoms, but they lack of course current contributions arising from τ. Figure 4 compares the aggregate relative SDs and relative MAEs for the entire test set obtained from these overall four treatments for several τ-dependent functionals (MN15-L, M06, MN15, and M06-2X are not shown, as their deviations would be too large to fit properly into the plots, see Tables S32 and S35 – S37). The statistical measures for individual nuclei are available in Tables S30 – S42 in the Supporting Information.

We note first of all, that the performances for τ_{MS}, τ_C, and τ_0 are generally very similar, while the τ_D CDFT results differ substantially from these data for several but not for all functionals. This suggests that the main differences do *not* arise from the τ_{MS} artifacts discussed further above, but that they reflect genuine current contributions provided by the τ_D CDFT framework. This outcome differs somewhat from previous analyses for main-group nuclei,[34,43,44] where sometimes the differences of τ_{MS} compared to τ_C and τ_0 were of similar magnitude as those relative to τ_D. The obvious reason for the large effects of explicit current contributions for some of the functionals in the present case seems to be the genuinely very large paratropic currents determining the shieldings and relative shifts for the transition-metal nuclei.

Indeed, for those functionals in Figure 4, where the differences between τ_D and the other three models are significant, the CDFT framework generally improves the agreement with experiment, as indicated by lower rel. SDs and rel. MAEs. This is particularly notable for the meta-GGAs M06-L, VSXC, B97M-V and SCAN: while all these functionals perform rather well, and the first two functionals were even the top performers for the entire test set, when used in their CDFT variants, they are much less convincing otherwise. Closer analyses (Tables S32 – S34) show that this holds for almost all nuclei, except for ^{53}Cr where the larger deshielding brought in by the CDFT contributions in fact deteriorates somewhat agreement with experiment, as was found for the main-group case.[34,43,44] For the three critical nuclei ^{55}Mn, ^{57}Fe, and ^{59}Co the improvements by

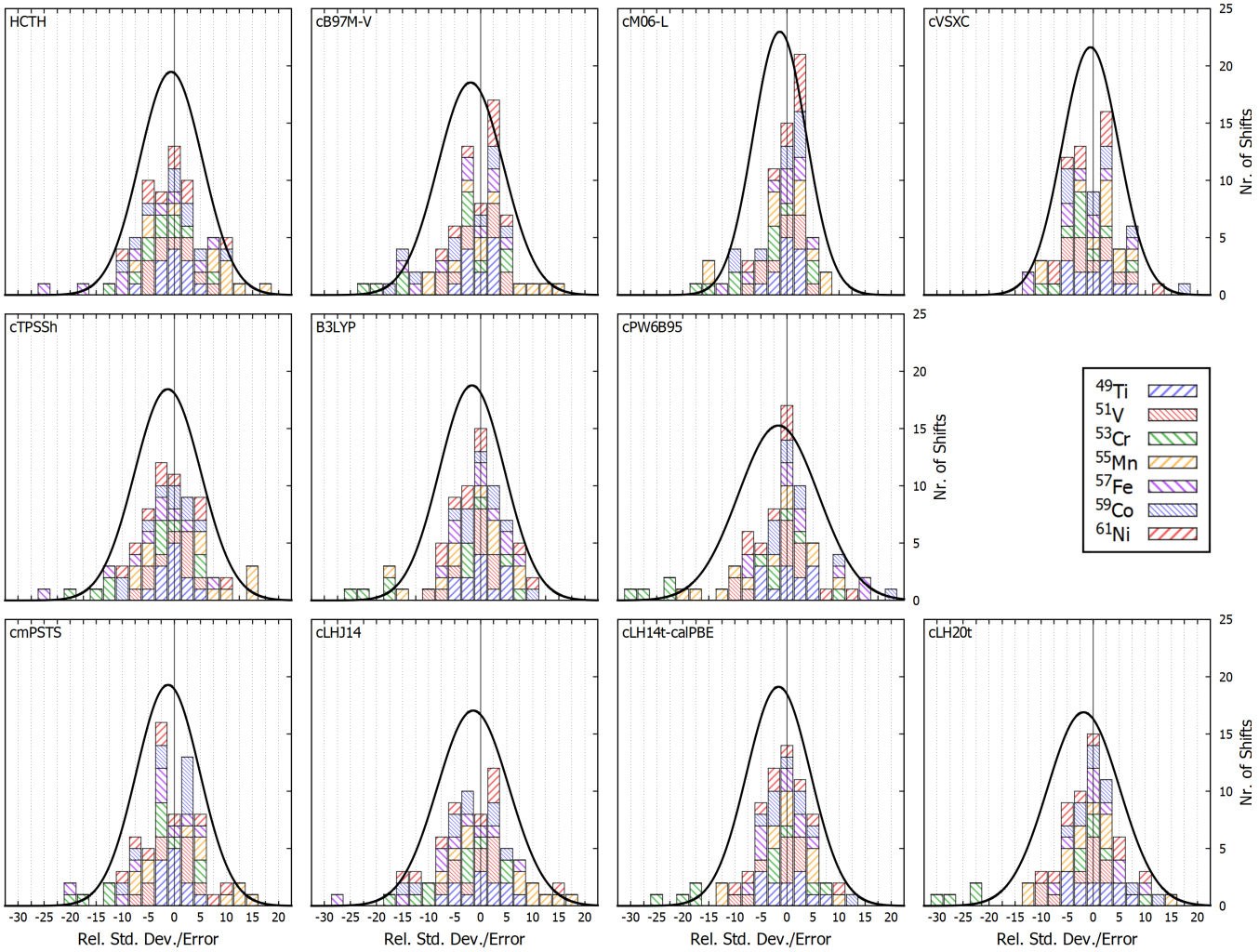

Figure 3: Standard deviation plots (solid black line) on top of histogram deviation plots of the individual 3d transition metal test sets ufor a larger selection of better-performing functionals within the range -45 % to +40 % in blocks of 5 %.

the CDFT terms are dramatic, to some extent comparable to the effects of moderate EXX admixture. Indeed, without the CDFT framework the best-performing meta-GGAs M06-L and VSXC (and partly B97M-V) would not offer any notable advantage over other semi-local functionals. Significant error reductions pertain also to SCAN. Smaller but still notable improvements are seen for TPSS, while the differences are very small for τ-HCTH.

For one meta-GGA not shown in Figure 4, MN15-L, the CDFT framework is actually overall detrimental to the agreement with experiment (Table S32). While cMN15-L improves somewhat over the other three schemes for ^{49}Ti, ^{51}V, ^{57}Fe, and ^{61}Ni, it gets significantly worse for ^{53}Cr, ^{55}Mn, and particularly for ^{59}Co. As a result, the overall rel. MAE increases from about 9%–10% for the other three schemes to about 13% for cMN15-L. It appears that here the current contributions overshoot for several nuclei, while they are more moderate and thus mostly improve matters for cM06-L or cVSXC (see above). This should be viewed against the backdrop that cMN15-L is strikingly improved over its non-CDFT variants for main-group shieldings, where it is in fact superior to both cM06-L and cVSXC.[34]

The performance of the two GHs TPSSh and PW6B95 also benefits very notably from the CDFT treatment, even though their EXX admixture does also bring in some current contributions. For TPSSh, the CDFT treatment gives slightly larger deviations for ^{53}Cr, which are outweighed by the improvements for the other nuclei. That is, the effects here also parallel those brought about by EXX admixture. For PW6B95 the improvements extend to essentially all nuclei except ^{61}Ni, which remains almost unaffected. Some improvements are found also for M06 (Table S35), even though the resulting deviations are still too large to fit the scale of Figure 4 (^{55}Mn shifts are improved most notably). In case of M06-2X and of MN15, the non-CDFT variants are even more strikingly worse than the already poorly performing CDFT variants. Indeed, for MN15 the deviations without CDFT treatment reach several hundreds of percent for the critical nuclei ^{55}Mn, ^{57}Fe, and ^{59}Co, suggesting extremely large current contributions needed to reach even moderately accurate results (Table S36). Nevertheless all of the just mentioned, highly parameterized, meta-GGA-based GHs are not competitive even when used in the CDFT framework.

The only RSH that depends on τ is ωB97M-V. Here the overall effects of the CDFT contributions are relatively small and tend to deteriorate the overall agreement with experiment slightly for most nuclei, except for ^{59}Co and ^{61}Ni (see Table S41). A smaller influence of the CDFT treatment is seen also for most LHs, and the overall effects may be somewhat favorable (LH20t) or very slightly unfa-

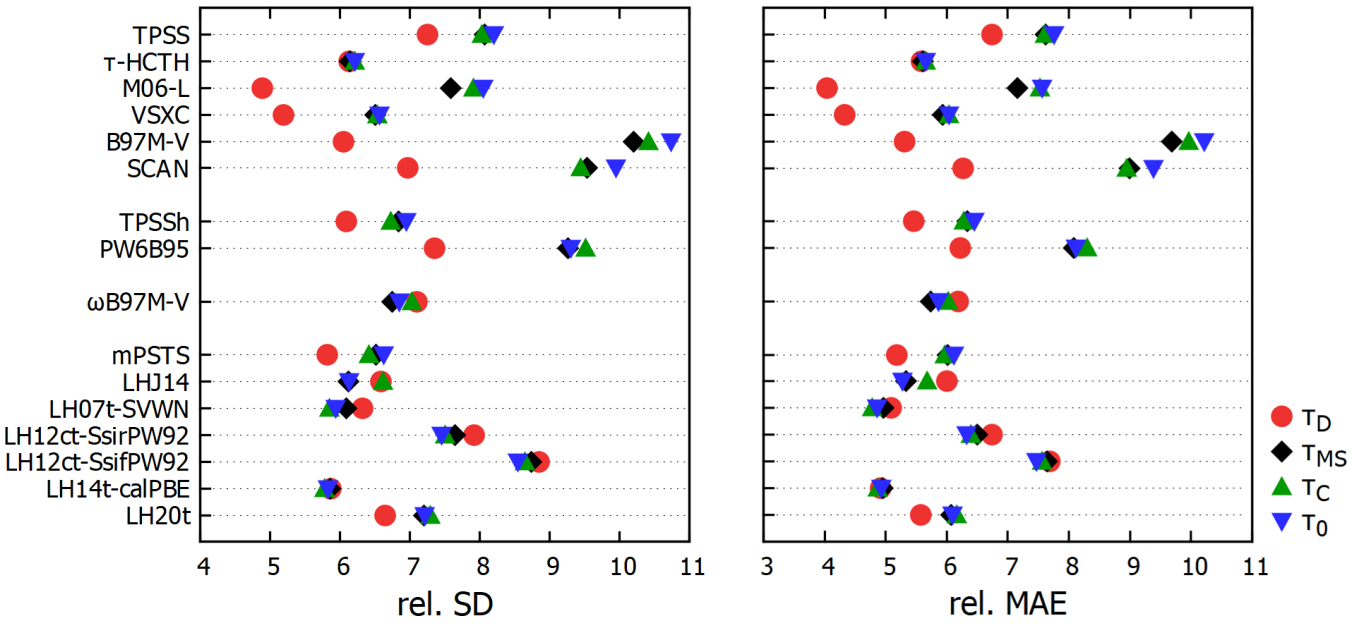

Figure 4: Effects of different treatments of τ on aggregate relative SDs and relative MAEs for different τ-dependent functionals.

vorable (LHJ14, LH07t-SVWN, LH12ct-SsirPW92, LH12ct-SsifPW92). Only mPSTS exhibits a larger improvement by the CDFT contributions for all nuclei except ^{61}Ni. For most LHs, we find moderate improvement for some nuclei and moderate deterioration for others adding up to the observed trend. LH20t shows small improvements for all nuclei, LH14t-calPBE exhibits generally negligible changes. The overall smaller effects of τ_D for most LHs are consistent with the argument that position-dependent EXX admixture, in particular in the core and semi-core regions around the NMR nucleus, helps to cover some current-dependencies that are absent for semi-local functionals or insufficiently described by most GHs.[43,44]

5 Conclusions

This report extends substantially earlier work on the quantum-chemical computation of the NMR chemical shifts of the 3d transition-metal nuclei. On one hand, the composed benchmark set covers 70 NMR shift values for both early and late 3d nuclei from ^{49}Ti, ^{51}V, ^{53}Cr, ^{55}Mn, ^{57}Fe, ^{59}Co, to ^{61}Ni. This provides a systematic comparative look at systems that so far had been evaluated separately at different levels. On the other hand, the overall 41 methods (plus different treatments of τ) evaluated here cover many approaches that had so far not been tested for transition-metal nuclei, in particular many more recent DFT methods. This includes current-density functional (CDFT) implementations of τ-dependent meta-GGAs and of other τ-dependent functionals based on Dobson's extension of τ in comparison with other treatments. In addition to a variety of semi-local functionals, a wide selection of global, range-separated, and local hybrid functionals have been compared, as well as Hartree-Fock, MP2 and two double-hybrid functionals. The same methods have recently been evaluated in an extended screening for main-group shieldings and shifts. In combination the two evaluations give an unprecedentedly detailed account of the performance of DFT methods for NMR shieldings and shifts.

One particularly striking result of the present study is, that two CDFT versions of meta-GGA functionals, cM06-L and cVSXC, are the top performers when evaluated across the entire 3d-nucleus test set. It appears that the CDFT-extension brings in advantages for the later nuclei ^{55}Mn, ^{57}Fe, ^{59}Co that otherwise can only be provided by moderate Hartree-Fock exchange admixtures in hybrid functionals. On the other hand, the disadvantages of Hartree-Fock exchange for ^{53}Cr are only partly mimicked by these functionals. In general, the effect of the CDFT extension of τ-dependent functionals can have a much larger effect in the present evaluations than for main-group nuclei. Performance is improved overall significantly (i.e. averaged over all nuclei), except for cMN15-L. This suggests that inclusion of current-dependence into a functional via τ contributions is particularly important for nuclei like ^{55}Mn, ^{57}Fe, ^{59}Co, which exhibit particularly large paratropic currents in their complexes.

Hartree-Fock admixture in different types of hybrid functionals may also be beneficial for these same nuclei for the same reason, i.e. to bring in current contributions. This is the case for moderate constant admixtures as in B3LYP, confirming the excellent performance of this functional for the later 3d nuclei (cTPSSh, B97-2, and partly cPW6B95, also belong to the better-performing global hybrids). But it holds also for several local hybrids, which also perform particularly well for these later nuclei. Too large Hartree-Fock exchange admixtures, either global, range-separated or local, deteriorate performance for ^{53}Cr. This can probably be traced back to triplet instabilities in high-oxidation-state complexes of these elements at Hartree-Fock level, and possibly to some lack of nuance in the ^{53}Cr set caused by experimental limitations. While most hybrid functionals do not show such instabilities, it seems that their remnants may still deteriorate the performance for the chromium subset increasingly with larger admixtures of Hartree-Fock exchange. Among the local hybrids, functionals with lower admixtures (cLH14t-calPBE, cLH07t-SVWN, cmPSTS) tend to perform best, changing somewhat the order of the best local hybrids compared to the main-group case. Some of the local hybrids, such as cLH14t-calPBE, may be particularly suitable for

multi-nuclear NMR studies on transition-metal complexes, where simultaneously high accuracy for metal and ligand shifts is desired.

Too high EXX admixtures in global or range-separated hybrids deteriorate even the behavior for the later 3d elements, where Hartree-Fock fails completely. MP2 cannot correct this and also is not applicable here, except for the uncritical ^{49}Ti case. MP2 contributions and large exact-exchange admixtures also make double hybrid functionals unsuitable for 3d transition-metal shifts, while some of them are known to be top performers in main-group shielding evaluations (in particular DSD-PBEP86). Overall, we can recommend cM06-L, cVSXC, cLH14t-calPBE, cLH07t-SVWN, cmPSTS, and B3LYP as particularly suitable functionals for 3d-nucleus NMR shifts. The systematic evaluation also provides hints for an even more fine-grained selection of methods for particular nuclei. These insights should be helpful in aiding NMR studies on transition-metal nuclei. In particular, an improved selection of methods for combined computational studies of metal and ligand NMR shifts in the context multi-nuclear NMR experiments should be enabled. The construction of more advanced local mixing functions for local hybrids is an area from which further improvements can be expected, including for heavier nuclei, where coordinate scaling in the high-density limit becomes important.

We close with a short take-home summary:

- Extended benchmark of experimental NMR shifts for 3d nuclei used to evaluate more than 40 DFT functionals from all rungs.
- Overall top performance found for current-density-response implementations of two meta-GGAs, cM06-L and cVSXC.
- This is followed closely by two local hybrids (LH14t-calPBE and LH07t-SVWN) and by the B3LYP global hybrid.
- Hartree-Fock, MP2 and double-hybrid functionals are completely unsuitable for the 3d shifts, except for ^{49}Ti, due to large static correlation effects and triplet instabilities.
- Some CDFT meta-GGAs and some local hybrids are suggested for multinuclear NMR studies on 3d transition-metal complexes.

Acknowledgement. C.J.S. is grateful for a scholarship which was provided by Studienstiftung des deutschen Volkes. This work has been funded by the German Research Foundation (Deutsche Forschungsgemeinschaft, DFG) within project KA1187/14-1. M.B. gratefully acknowledges support from EaStCHEM and the School of Chemistry in St Andrews.

Supporting Information Available

The Supporting Information contains a list of the experimental data used, the comparison of shift results with BP86-D3(BJ)/def2-TZVP(D) and TPSSh-D3(BJ)/def2-TZVP(D) structures for a subset of functionals, estimates of solvent effects on the shifts of some selected complexes, evaluation of UKS solutions for triplet-unstable BHLYP wavefunctions using ORCA in comparison to RKS values with ORCA and TURBOMOLE, estimates of scalar relativistic effects for all complexes with the best performing cM06-L functional, shieldings, shifts and statistical results for non-truncated vs. model complexes (see text), mean statistical data for the Y-intercept vs referenced shift calculations, as well as full shifts, shieldings and statistical results for all functionals, including all τ-models with BP86-D3(BJ)/def2-TZVP(D) structures, as well as comparisons of relevant structural parameters of the BP86-D3(BJ)/def2-TZVP(D) and TPSSh-D3(BJ)/def2-TZVP(D) structures and the Cartesian input files for all complexes of the present study. This material is available free of charge via the Internet at http://pubs.acs.org.

References

(1) Proctor, W. G.; Yu, F. C. On the Nuclear Magnetic Moments of Several Stable Isotopes. *Phys. Rev.* **1951**, *81*, 20–30.

(2) Mason, J. *Multinuclear NMR*; Plenum Press: New York, 1987.

(3) Werhun, P.; Bryce, D. L. Structural and Crystallographic Information from ^{61}Ni Solid-State NMR Spectroscopy: Diamagnetic Nickel Compounds. *Inorg. Chem.* **2017**, *56*, 9996–10006.

(4) Autschbach, J. In *Principles and Applications of Density Functional Theory in Inorganic Chemistry I*; Kaltsoyannis, N., McGrady, J. E., Eds.; Structure and Bonding; Springer: Heidelberg, 2004; Vol. 112; pp 1–43.

(5) Flaig, D.; Maurer, M.; Hanni, M.; Braunger, K.; Kick, L.; Thubauville, M.; Ochsenfeld, C. Benchmarking Hydrogen and Carbon NMR Chemical Shifts at HF, DFT, and MP2 Levels. *J. Chem. Theory Comput.* **2014**, *10*, 572–578.

(6) Maurer, M.; Ochsenfeld, C. Spin Component-Scaled Second-Order Møller-Plesset Perturbation Theory for Calculating NMR Shieldings. *J. Chem. Theory Comput.* **2015**, *11*, 37–44.

(7) Kaupp, M.; Bühl, M.; Malkin, V. G. *Calculation of NMR and EPR Parameters*, 1st ed.; Wiley-VCH: Weinheim, 2004.

(8) Schreckenbach, G.; Ziegler, T. Density functional calculations of NMR chemical shifts and ESR g-tensors. *Theor. Chem. Acc.* **1998**, *99*, 71–82.

(9) Bühl, M.; Kaupp, M.; Malkina, O. L.; Malkin, V. G. The DFT Route to NMR Chemical Shifts. *J. Comp. Chem.* **1999**, *20*, 91–105.

(10) Kaupp, M.; Bühl, M. In *Computational Inorganic and Bioinorganic Chemistry*; Solomon, E., King, R. B., Scott, R. A., Eds.; Encyclopedia of Inorganic Chemistry; Wiley: Chichester, 2009; pp 91–107.

(11) Kaupp, M.; Malkina, O. L.; Malkin, V. G. In *Encyclopedia of Computational Chemistry*; Schleyer, P. v. R., Ed.; Wiley Interscience: New York, 1998; pp 1857–1866.

(12) Bühl, M. In *Annual Reports on NMR Spectroscopy*; Webb, G. A., Ed.; Academic Press: The Netherlands, 2008; Vol. 64; pp 77–126.

(13) Autschbach, J. Density functional theory applied to calculating optical and spectroscopic properties of metal complexes: NMR and optical activity. *Coord. Chem. Rev.* **2007**, *251*, 1796–1821.

(14) Chan, J. C. C.; Au-Yeung, S. C. F. Density Functional Study of ^{59}Co Chemical Shielding Tensors Using Gauge-Including Atomic Orbitals. *J. Phys. Chem. A* **1997**, *101*, 3637–3640.

(15) Bühl, M. Density functional computations of transition metal NMR chemical shifts: dramatic effects of Hartree-Fock exchange. *Chem. Phys. Lett.* **1997**, *267*, 251–257.

(16) Grigoleit, S.; Bühl, M. Computational ^{59}Co NMR Spectroscopy: Beyond Static Molecules. *J. Chem. Theory Comput.* **2005**, *1*, 181–193.

(17) Bühl, M. Density functional computation of ^{55}Mn NMR parameters. *Theor. Chem. Acc.* **2002**, *107*, 336–342.

(18) Bühl, M.; Peters, D.; Herges, R. Substituent effects on ^{61}Ni NMR chemical shifts. *Dalton Trans.* **2009**, 6037–6044.

(19) Bühl, M.; Gaemers, S.; Elsevier, C. J. Density-Functional Computation of ^{99}Ru NMR Parameters. *Chem. Eur. J.* **2000**, *6*, 3272–3280.

(20) Bühl, M.; Mikael Håkansson, M.; Mahmoudkhani, A. H.; Öhrström, L. X-ray Structures and DFT Calculations on Rhodium-Olefin Complexes: Comments on the ^{103}Rh NMR Shift-Stability Correlation. *Organometallics* **2000**, *19*, 5589–5596.

(21) Ramalho, T. C.; Bühl, M.; Figueroa-Villar, J. D.; de Alencastro, R. B. Computational NMR Spectroscopy of Transition-Metal/Nitroimidazole Complexes: Theoretical Investigation of Potential Radiosensitizers. *Helv. Chim. Acta* **2005**, *88*, 2705–2721.

(22) Kaupp, M.; Reviakine, R.; Malkina, O. L.; Arbuznikov, A.; Schimmelpfennig, B.; Malkin, V. G. Calculation of electronic g-tensors for transition metal complexes using hybrid density functionals and atomic meanfield spin-orbit operators. *J. Comp. Chem.* **2002**, *23*, 794–803.

(23) Frantz, S.; Hartmann, H.; Doslik, N.; Wanner, M.; Kaim, W.; Kümmerer, H.-J.; Denninger, G.; Barra, A.-L.; Duboc-Toia, C.; Fiedler, J.; Ciofini, I.; Urban, C.; Kaupp, M. Multifrequency EPR Study and Density Functional g-Tensor Calculations of Persistent Organorhenium Radical Complexes. *J. Am. Chem. Soc.* **2002**, *124*, 10563–10571.

(24) Schreckenbach, G. The ^{57}Fe nuclear magnetic resonance shielding in ferrocene revisited. A density-functional study of orbital energies, shielding mechanisms, and the influence of the exchange-correlation functional. *J. Chem. Phys.* **1999**, *110*, 11936–11949.

(25) Bühl, M. Density Functional Calculations of ^{95}Mo NMR Chemical Shifts: Applications to Model Catalysts for Imine Metathesis. *Chem. Eur. J.* **1999**, *5*, 3514–3522.

(26) Bühl, M.; Golubnychiy, V. Density-functional computation of ^{99}Tc NMR chemical shifts. *Magn. Reson. Chem.* **2008**, *46*, S36–S44.

(27) Bühl, M. Density-functional computation of ^{53}Cr NMR chemical shifts. *Magn. Reson. Chem.* **2006**, *44*, 661–668.

(28) Bühl, M.; Mauschick, F. T. Density functional computation of ^{49}Ti NMR chemical shifts. *Magn. Reson. Chem.* **2004**, *42*, 737–744.

(29) Bühl, M.; Hamprecht, F. A. Theoretical Investigations of NMR Chemical Shifts and Reactivities of Oxovanadium(V) Compounds. *J. Comput. Chem.* **1998**, *19*, 113–122.

(30) Bühl, M. NMR Chemical Shifts of Zr@C28. How Shielded Can ^{91}Zr Get? *J. Phys. Chem. A* **1997**, *101*, 2514–2517.

(31) Kupka, T. H_2O, H_2, HF, F_2 and F_2O nuclear magnetic shielding constants and indirect nuclear spin-spin coupling constants (SSCCs) in the BHandH/pcJ-n and BHandH/XZP Kohn–Sham limits. *J. Chem. Theory Comput.* **2009**, *47*, 959–970.

(32) Stoychev, G. L.; Auer, A. A.; Neese, F. Efficient and Accurate Prediction of Nuclear Magnetic Resonance Shielding Tensors with Double-Hybrid Density Functional Theory. *J. Chem. Theory Comput.* **2018**, *14*, 4756–4771.

(33) Schattenberg, C. J.; Reiter, K.; Weigend, F.; Kaupp, M. An Efficient Coupled-Perturbed Kohn–Sham Implementation of NMR Chemical Shift Computations with Local Hybrid Functionals and Gauge-Including Atomic Orbitals. *J. Chem. Theory Comput.* **2020**, *16*, 931–943.

(34) Schattenberg, C. J.; Kaupp, M. Extended Benchmark Set of Main-Group Nuclear Shielding Constants and NMR Chemical Shifts and Its Use to Evaluate Modern DFT Methods. *J. Chem. Theory Comput.* **2021**, DOI:10.1021/acs.jctc.1c00919.

(35) Srebro, M.; Autschbach, J. Computational Analysis of $^{47/49}$Ti NMR Shifts and Electric Field Gradient Tensors of Half-Titanocene Complexes: Structure–Bonding–Property Relationships. *Chem. Eur. J.* **2013**, *19*, 12018–12033.

(36) Lee, J.; Head-Gordon, M. Distinguishing artificial and essential symmetry breaking in a single determinant: approach and application to the C_{60}, C_{36}, and C_{20} fullerenes. *Phys. Chem. Chem. Phys.* **2019**, *21*, 4763–4778.

(37) Shee, J.; Loipersberger, M.; Hait, D.; Lee, J.; Head-Gordon, M. Revealing the nature of electron correlation in transition metal complexes with symmetry breaking and chemical intuition. *J. Chem. Phys.* **2021**, *154*, 194109.

(38) Maier, T. M.; Arbuznikov, A. V.; Kaupp, M. Local hybrid functionals: Theory, implementation, and performance of an emerging new tool in quantum chemistry and beyond. *WIREs Comp. Mol. Sci.* **2019**, *9*, e1378.

(39) Arbuznikov, A. V.; Kaupp, M. Nuclear shielding constants from localized local hybrid exchange-correlation potentials. *Chem. Phys. Lett.* **2007**, *442*, 496–503.

(40) Teale, A. M.; Tozer, D. J. Exchange representations in Kohn–Sham NMR shielding calculations. *Chem. Phys. Lett.* **2004**, *383*, 109–114.

(41) Wilson, P. J.; Tozer, D. J. Varying the fraction of orbital exchange in density functional theory: Influence on nuclear magnetic resonance shielding constants. *J. Chem. Phys.* **2002**, *116*, 10139–10147.

(42) Reimann, S.; Ekström, U.; Stopkowicz, S.; Teale, A. M.; Borgoo, A.; Helgaker, T. The importance of current contributions to shielding constants in density-functional theory. *Phys. Chem. Chem. Phys.* **2015**, *17*, 18834–18842.

(43) Schattenberg, C. J.; Kaupp, M. Effect of the Current Dependence of Tau-Dependent Exchange-Correlation Functionals on Nuclear Shielding Calculations. *J. Chem. Theory Comput.* **2021**, *17*, 1469–1479.

(44) Schattenberg, C. J.; Kaupp, M. Implementation and Validation of Local Hybrid Functionals with Calibrated Exchange-Energy Densities for Nuclear Shielding Constants. *J. Phys. Chem. A* **2021**, *125*, 2697–2707.

(45) Maximoff, S. N.; Scuseria, G. E. Nuclear magnetic resonance shielding tensors calculated with kinetic energy density-dependent exchange-correlation functionals. *Chem. Phys. Lett.* **2004**, *390*, 408–412.

(46) Dobson, J. F. Spin-density functionals for the electron correlation energy with automatic freedom from orbital self-interaction. *J. Phys.: Condens. Matter* **1992**, *4*, 7877–7890.

(47) Bates, J. E.; Furche, F. Harnessing the meta-generalized gradient approximation for time-dependent density functional theory. *J. Chem. Phys.* **2012**, *137*, 164105.

(48) Becke, A. D. Current density in exchange-correlation functionals: Application to atomic states. *J. Chem. Phys.* **2002**, *117*, 6935–6938.

(49) Tao, J. Explicit inclusion of paramagnetic current density in the exchange-correlation functionals of current-density functional theory. *Phys. Rev. B* **2005**, *71*, 205107.

(50) Haasler, M.; Maier, T. M.; Grotjahn, R.; Gückel, S.; Arbuznikov, A. V.; Kaupp, M. A Local Hybrid Functional with Wide Applicability and Good Balance between (De)Localization and Left-Right Correlation. *J. Chem. Theory Comput.* **2020**, *16*, 5645–5657.

(51) Holzer, C.; Franzke, Y. J.; Kehry, M. Assessing the Accuracy of Local Hybrid Density Functional Approximations for Molecular Response Properties. *J. Chem. Theory Comput.* **2021**, *17*, 2928–2947.

(52) Perdew, J. P.; Staroverov, V. N.; Tao, J.; Scuseria, G. E. Density functional with full exact exchange, balanced nonlocality of correlation, and constraint satisfaction. *Phys. Rev. A.* **2008**, *78*, 052513.

(53) Johnson, E. R. Local-hybrid functional based on the correlation length. *J. Chem. Phys.* **2014**, *141*, 124120.

(54) Perdew, J. P.; Schmidt, K. Jacob's ladder of density functional approximations for the exchange-correlation energy. *AIP Conf. Proc.* **2001**, *577*, 1–20.

(55) Kozuch, S.; Martin, J. M. L. DSD-PBEP86: In search of the best double-hybrid DFT with spin-component scaled MP2 and dispersion corrections. *Phys. Chem. Chem. Phys.* **2011**, *13*, 20104–20107.

(56) Kozuch, S.; Martin, J. M. L. Spin-Component-Scaled Double Hybrids: An Extensive Search for the Best Fifth-Rung Functionals Blending DFT and Perturbation Theory. *J. Comput. Chem.* **2013**, *34*, 2327–2344.

(57) Wodyński, A.; Kaupp, M. Noncollinear Relativistic Two-Component X2C Calculations of Hyperfine Couplings Using Local Hybrid Functionals. Importance of the High-Density Coordinate Scaling Limit. *J. Chem. Theory Comput.* **2020**, *16*, 314–325.

(58) Kaupp, M. The role of radial nodes of atomic orbitals for chemical bonding and the periodic table. *J. Comp. Chem.* **2007**, *28*, 320–325.

(59) Joy, J.; Danovich, D.; Kaupp, M.; Shaik, S. A Unified Understanding on the Covalent vs. Charge-Shift Nature of the Metal-Metal Bond in Transition Metal Complexes. *J. Am. Chem. Soc.* **2020**, *142*, 12277–12287.

(60) Furness, J. W.; Verbeke, J.; Tellgren, E. I.; Stopkowicz, S.; Ekström, U.; Helgaker, T.; Teale, A. M. Current Density Functional Theory Using Meta-Generalized Gradient Exchange-Correlation Functionals. *J. Chem. Theory Comput.* **2015**, *11*, 4169–4181.

(61) Irons, T. J. P.; Spence, L.; David, G.; Speake, B. T.; Helgaker, T.; Teale, A. M. Analyzing Magnetically Induced Currents in Molecular Systems Using Current-Density-Functional Theory. *J. Phys. Chem. A* **2020**, *124*, 1321–1333.

(62) Franzke, Y. J.; Mack, F.; Weigend, F. NMR Indirect Spin–Spin Coupling Constants in a Modern Quasirelativistic Density Functional Framework. *J. Chem. Theory Comput.* **2021**, *17*, 3974–3994.

(63) Neese, F. Software update: the ORCA program system, version 4.0. *Wiley Interdisciplinary Reviews: Computational Molecular Science* **2017**, *8*, e1327.

(64) Neese, F.; Wennmohs, F.; Becker, U.; Riplinger, C. The ORCA quantum chemistry program package. *J. Chem. Phys.* **2020**, *152*, 224108.

(65) Stoychev, G. L.; Auer, A. A.; Izsàk, R.; Neese, F. Self-Consistent Field Calculation of Nuclear Magnetic Resonance Chemical Shielding Constants Using Gauge-Including Atomic Orbitals and Approximate Two-Electron Integrals. *J. Chem. Theory Comput.* **2018**, *14*, 619–637.

(66) Local version derived from TURBOMOLE version 7.5, TURBOMOLE GmbH, 2020. TURBOMOLE is a development of University of Karlsruhe and Forschungszentrum Karlsruhe 1989-2007, TURBOMOLE GmbH since 2007.

(67) Balasubramani, S. G.; Chen, G. P.; Coriani, S.; Diedenhofen, M.; Frank, M. S.; Franzke, Y. J.; Furche, F.; Grotjahn, R.; Harding, M. E.; Hättig, C.; et al., TURBOMOLE. *J. Chem. Phys.* **2020**, *152*, 184107.

(68) Weigend, F.; Ahlrichs, R. Balanced basis sets of split valence, triple zeta valence and quadruple zeta valence quality for H to Rn: Design and assessment of accuracy. *Phys. Chem. Chem. Phys.* **2005**, *7*, 3297–3305.

(69) Rappoport, D.; Furche, F. Property-optimized Gaussian basis sets for molecular response calculations. *J. Chem. Phys.* **2010**, *133*, 134105.

(70) Staroverov, V. N.; Scuseria, G. E.; Tao, J.; Perdew, J. P. Comparative assessment of a new nonempirical density functional: Molecules and hydrogen-bonded complexes. *J. Chem. Phys.* **2003**, *119*, 12129–12137.

(71) Grimme, S.; Antony, J.; Ehrlich, S.; Krieg, H. A consistent and accurate ab initio parametrization of density functional dispersion correction (DFT-D) for the 94 elements H-Pu. *J. Chem. Phys.* **2010**, *132*, 154104.

(72) Grimme, S.; Ehrlich, S.; Goerigk, L. Effect of the damping function in dispersion corrected density functional theory. *J. Comput. Chem.* **2011**, *32*, 1456–1465.

(73) Becke, A. D.; Johnson, E. R. A density-functional model of the dispersion interaction. *J. Chem. Phys.* **2005**, *123*, 154101.

(74) Johnson, E. R.; Becke, A. D. A post-Hartree-Fock model of intermolecular interactions. *J. Chem. Phys.* **2005**, *123*, 024101.

(75) Johnson, E. R.; Becke, A. D. A post-Hartree-Fock model of intermolecular interactions: Inclusion of higher-order corrections. *J. Chem. Phys.* **2006**, *124*, 174104.

(76) Feher, F. J.; Blanski, R. L. Lewis Acid Adducts of Oxovanadium(V) Alkyl and Triphenylsiloxy Complexes: Synthesis, Characterization, and Reactivity toward Ethylene. *Organometallics* **1993**, *12*, 958–963.

(77) Koller, M. W. CO-Austauschreaktionen an Metallcarbonyl(Olefin)-Komplexen: I. Synthese optisch aktiver Organoeisenkomplexe; II. Korrelation zwischen Metallkernresonanz und Reaktivität. Dissertation, Universität Zürich, 1993.

(78) Grimme, S. Exploration of Chemical Compound, Conformer, and Reaction Space with Meta-Dynamics Simulations Based on Tight-Binding Quantum Chemical Calculations. *J. Chem. Theory Comput.* **2019**, *15*, 2847–2862.

(79) Pracht, P.; Bohle, F.; Grimme, S. Automated exploration of the low-energy chemical space with fast quantum chemical methods. *Phys. Chem. Chem. Phys.* **2020**, *22*, 7169–7192.

(80) London, F. Théorie quantique des courants interatomiques dans les combinaisons aromatiques. *J. Phys. Radium* **1937**, *8*, 397–409.

(81) Ditchfield, R. Self-consistent perturbation theory of diamagnetism. *Mol. Phys.* **1974**, *27*, 789–807.

(82) Wolinski, K.; Hinton, J. F.; Pulay, P. Efficient Implementation of the Gauge-Independent Atomic Orbital Method for NMR Chemical Shift Calculations. *J. Am. Chem. Soc.* **1990**, *112*, 8251–8260.

(83) Jensen, F. Segmented Contracted Basis Sets Optimized for Nuclear Magnetic Shielding. *J. Chem. Theory Comput.* **2015**, *11*, 132–138.

(84) CFOUR, a quantum chemical program package written by J.F. Stanton, J. Gauss, L. Cheng, M.E. Harding, D.A. Matthews, P.G. Szalay, with contributions from A.A. Auer, R.J. Bartlett, U. Benedikt, C. Berger, D.E. Bernholdt, Y.J. Bomble, O. Christiansen, F. Engel, R. Faber, M. Heckert, O. Heun, M. Hilgenberg, C. Huber, T.-C. Jagau, D. Jonsson, J. Jusélius, T. Kirsch, K. Klein, W.J. Lauderdale, F. Lipparini, T. Metzroth, L.A. Mück, D.P. O'Neill, D.R. Price, E. Prochnow, C. Puzzarini, K. Ruud, F. Schiffmann, W. Schwalbach, C. Simmons, S. Stopkowicz, A. Tajti, J. Vázquez, F. Wang, J.D. Watts and the integral packages MOLECULE (J. Almlöf and P.R. Taylor), PROPS (P.R. Taylor), ABACUS (T. Helgaker, H.J. Aa. Jensen, P. Jørgensen, and J. Olsen), and ECP routines by A. V. Mitin and C. van Wüllen. For the current version, see http://www.cfour.de.

(85) Weigend, F. Accurate Coulomb-fitting basis sets for H to Rn. *Phys. Chem. Chem. Phys.* **2006**, *8*, 1057–1065.

(86) Weigend, F. Hartree–Fock exchange fitting basis sets for H to Rn. *J. Comput. Chem.* **2008**, *29*, 167–175.

(87) Stoychev, G. L.; Auer, A. A.; Neese, F. Automatic Generation of Auxiliary Basis Sets. *J. Chem. Theory Comput.* **2017**, *13*, 554–562.

(88) Bühl, M.; Parrinello, M. Medium Effects on ^{51}V NMR Chemical Shifts: A Density Functional Study. *Chem. Eur. J.* **2001**, *7*, 4487–4494.

(89) Bühl, M.; Mauschick, F. T. Thermal and solvent effects on ^{57}Fe NMR chemical shifts. *Phys. Chem. Chem. Phys.* **2002**, *4*, 5508–5514.

(90) Bühl, M.; Mauschick, F. T.; Terstegen, F.; Wrackmeyer, B. Remarkably Large Geometry Dependence of ^{57}Fe NMR Chemical Shifts. *Angew. Chem. Int. Ed.* **2002**, *41*, 2312–2315.

(91) Bühl, M.; Grigoleit, S.; Kabrede, H.; Mauschick, T. Simulation of ^{59}Co NMR Chemical Shifts in Aqueous Solution. *Chem. Eur. J.* **2006**, *12*, 477–488.

(92) Franzke, Y. J.; Weigend, F. NMR Shielding Tensors and Chemical Shifts in Scalar-Relativistic Local Exact Two-Component Theory. *J. Chem. Theory Comput.* **2019**, *15*, 1028–1043.

(93) Vícha, J.; Novotný, J.; Komorovsky, S.; Straka, M.; Kaupp, M.; Marek, R. Relativistic Heavy-Neighbor-Atom Effects on NMR Shifts: Concepts and Trends Across the Periodic Table. *Chem. Rev.* **2020**, *120*, 7065–7103.

(94) Kaupp, M.; Malkina, O. L.; Malkin, V. G.; Pyykkö, P. How Do Spin-Orbit-Induced Heavy-Atom Effects on NMR Chemical Shifts Function? Validation of a Simple Analogy to Spin-Spin Coupling by Density Functional Theory (DFT) Calculations on Some Iodo Compounds. *Chem. Eur. J.* **1998**, *4*, 118–126.

(95) Kaupp, M. In *Relativistic Electronic Structure Theory II: Applications*; Schwerdtfeger, P., Ed.; series Theoretical and Computational Chemistry; Elsevier: Amsterdam, 2004; Chapter 9, pp 552–597.

(96) Slater, J. C. A Simplification of the Hartree–Fock Method. *Phys. Rev.* **1951**, *81*, 385–390.

(97) Vosko, S. H.; Wilk, L.; Nusair, M. Accurate spin-dependent electron liquid correlation energies for local spin density calculations: a critical analysis. *Can. J. Phys.* **1980**, *58*, 1200–1211.

(98) Becke, A. D. Density-functional exchange-energy approximation with correct asymptotic behavior. *Phys. Rev. A* **1988**, *38*, 3098–3100.

(99) Lee, C.; Yang, W.; Parr, R. G. Development of the Colle-Salvetti correlation-energy formula into a functional of the electron density. *Phys. Rev. B* **1988**, *37*, 785–789.

(100) Perdew, J. P. Density-functional approximation for the correlation energy of the inhomogeneous electron gas. *Phys. Rev. B* **1986**, *33*, 8822–8824.

(101) Perdew, J. P. Erratum: Density-functional approximation for the correlation energy of the inhomogeneous electron gas. *Phys. Rev. B* **1986**, *34*, 7406.

(102) Perdew, J. P.; Burke, K.; Ernzerhof, M. Generalized Gradient Approximation Made Simple. *Phys. Rev. Lett.* **1996**, *77*, 3865–3868.

(103) Keal, T. W.; Tozer, D. J. The exchange-correlation potential in Kohn–Sham nuclear magnetic resonance shielding calculations. *J. Chem. Phys.* **2003**, *119*, 3015–3024.

(104) Keal, T. W.; Tozer, D. J. A semiempirical generalized gradient approximation exchange-correlation functional. *J. Chem. Phys.* **2004**, *121*, 5654–5660.

(105) Grimme, S. Semiempirical GGA-Type Density Functional Constructed with a Long-Range Dispersion Correction. *J. Comp. Chem.* **2006**, *27*, 1787–1799.

(106) Hamprecht, F. A.; Cohen, A. J.; Tozer, D. J.; Handy, N. C. Development and assessment of new exchange-correlation functionals. *J. Chem. Phys.* **1998**, *109*, 6264–6271.

(107) Boese, A. D.; Handy, N. C. A new parametrization of exchange-correlation generalized gradient approximation functionals. *J. Chem. Phys.* **2001**, *114*, 5497–5503.

(108) Tao, J.; Perdew, J. P.; Staroverov, V. N.; Scuseria, G. E. Climbing the Density Functional Ladder: Nonempirical Meta-Generalized Gradient Approximation Designed for Molecules and Solids. *Phys. Rev. Lett.* **2003**, *91*, 146401.

(109) Zhao, Y.; Truhlar, D. G. A new local density functional for main-group thermochemistry, transition metal bonding, thermochemical kinetics, and noncovalent interactions. *J. Chem. Phys.* **2006**, *125*, 194101.

(110) Yu, H. S.; He, X.; Truhlar, D. G. MN15-L: A New Local Exchange-Correlation Functional for Kohn–Sham Density Functional Theory with Broad Accuracy for Atoms, Molecules, and Solids. *J. Chem. Theory Comput.* **2016**, *12*, 1280–1293.

(111) Van Voorhis, T.; Scuseria, G. E. A novel form for the exchange-correlation energy functional. *J. Chem. Phys.* **1998**, *109*, 400–410.

(112) Boese, A. D.; Handy, N. C. New exchange-correlation density functionals: The role of the kinetic-energy density. *J. Chem. Phys.* **2002**, *116*, 9559–9569.

(113) Mardirossian, N.; Head-Gordon, M. Mapping the genome of meta-generalized gradient approximation density functionals: The search for B97M-V. *J. Chem. Phys.* **2015**, *142*, 074111.

(114) Sun, J.; Ruzsinszky, A.; Perdew, J. P. Strongly Constrained and Appropriately Normed Semilocal Density Functional. *Phys. Rev. Lett.* **2015**, *115*, 036402.

(115) Becke, A. D. Density-functional thermochemistry. III. *J. Chem. Phys.* **1993**, *98*, 5648–5652.

(116) Adamo, C.; Barone, V. Toward reliable density functional methods without adjustable parameters: The PBE0 model. *J. Chem. Phys.* **1999**, *110*, 6158–6170.

(117) Wilson, P. J.; Bradley, T. J.; Tozer, D. J. Hybrid exchange-correlation functional determined from thermochemical data and *ab initio* potentials. *J. Chem. Phys.* **2001**, *115*, 9233–9242.

(118) Becke, A. D. A new mixing of Hartree-Fock and local density-functional theories. *J. Chem. Phys.* **1993**, *98*, 1372–1377.

(119) Zhao, Y.; Truhlar, D. G. Design of Density Functionals That Are Broadly Accurate for Thermochemistry, Thermochemical Kinetics, and Nonbonded Interactions. *J. Phys. Chem. A* **2005**, *109*, 5656–5667.

(120) Zhao, Y.; Truhlar, D. G. The M06 suite of density functionals for main group thermochemistry, thermochemical kinetics, noncovalent interactions, excited states, and transition elements: two new functionals and systematic testing of four M06-class functionals and 12 other functionals. *Theor. Chem. Acc.* **2008**, *120*, 215–241.

(121) Yu, H. S.; He, X.; Li, S. L.; Truhlar, D. G. MN15: A Kohn-Sham global-hybrid exchange-correlation density functional with broad accuracy for multi-reference and single-reference systems and noncovalent interactions. *Chem. Sci.* **2016**, *7*, 5032–5051.

(122) Yanai, T.; Tew, D. P.; N. Handy, N. C. A new hybrid exchange-correlation functional using the Coulomb-attenuating method (CAM-B3LYP). *Chem. Phys. Lett.* **2004**, *393*, 51–57.

(123) Chai, J.-D.; Head-Gordon, M. Long-range corrected hybrid density functionals with damped atom-atom dispersion corrections. *Phys. Chem. Chem. Phys.* **2008**, *10*, 6615–6620.

(124) Mardirossian, N.; Head-Gordon, M. ωB97X-V: A 10-parameter, range-separated hybrid, generalized gradient approximation density functional with nonlocal correlation, designed by a survival-of-the-fittest strategy. *Phys. Chem. Chem. Phys.* **2014**, *16*, 9904–9924.

(125) Mardirossian, N.; Head-Gordon, M. ωB97M-V: A combinatorially optimized, range-separated hybrid, meta-GGA density functional with VV10 nonlocal correlation. *J. Chem. Phys.* **2016**, *144*, 214110.

(126) Arbuznikov, A. V.; Kaupp, M. Local hybrid exchange-correlation functionals based on the dimensionless density gradient. *Chem. Phys. Lett.* **2007**, *440*, 160–168.

(127) Kaupp, M.; Bahmann, H.; Arbuznikov, A. V. Local hybrid functionals: An assessment for thermochemical kinetics. *J. Chem. Phys.* **2007**, *127*, 194102.

(128) Arbuznikov, A. V.; Kaupp, M. Importance of the correlation contribution for local hybrid functionals: Range separation and self-interaction corrections. *J. Chem. Phys.* **2012**, *136*, 014111.

(129) Arbuznikov, A. V.; Kaupp, M. Towards improved local hybrid functionals by calibration of exchange-energy densities. *J. Chem. Phys.* **2014**, *141*, 204101.

(130) Møller, C.; Plesset, M. S. Note on an approximation treatment for many-electron systems. *Phys. Rev.* **1934**, *46*, 618–622.

(131) Grimme, S. Semiempirical hybrid density functional with perturbative second-order correlation. *J. Chem. Phys.* **2006**, *124*, 034108.

(132) Bühl, M.; Kabrede, H. Geometries of Transition-Metal Complexes from Density-Functional Theory. *J. Chem. Theroy Comput.* **2006**, *2*, 1282–1290.

(133) Schattenberg, C. J.; Maier, T.; Kaupp, M. Lessons from the Spin-Polarization/Spin-Contamination Dilemma of Transition-Metal Hyperfine Couplings for the Construction of Exchange-Correlation Functionals. *J. Chem. Theory. Comput.* **2018**, *14*, 5653–5672.

(134) Bühl, M.; Wrackmeyer, B. Density-functional computation of ^{93}Nb NMR chemical shifts. *Magn. Reson. Chem.* **2010**, *48*, 561–568.

(135) Wilson, P. J.; Amos, R. D.; Handy, N. C. Density functional predictions for metal and ligand nuclear shielding constants in diamagnetic closed-shell first-row transition-metal complexes. *Phys. Chem. Chem. Phys.* **2000**, *2*, 187–194.

(136) Benn, R.; Rufińska, A. Indirect Two-Dimensional Heteronuclear NMR Spectroscopy of Low-γ Metal Nuclei (M = ^{183}W, ^{57}Fe, ^{103}Rh, ^{61}Ni). *Magn. Reson. Chem.* **1988**, *26*, 895–902.

(137) Hafner, A.; Hegedus, L. S.; deWeck, G.; Hawkins, B.; Dötz, K. H. Chromium-53 Nuclear Magnetic Resonance Studies of Pentacarbonylchromium-Carbene Complexes. *J. Am. Chem. Soc.* **1988**, *110*, 8413–8421.

(138) Berger, S.; Bock, W.; Frenking, G.; Jonas, V.; Müller, F. NMR Data of Methyltitanium Trichloride and Related Organometallic Compounds, A Combined Experimental and Theoretical Study of Me_nXCl_{4-n} (n = 0—4; X = C, Si, Sn, Pb, Ti). *J. Am. Chem. Soc.* **1995**, *117*, 3820–3829.

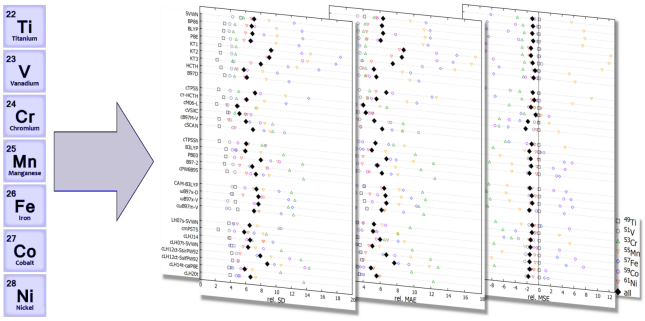
22 Ti Titanium
23 V Vanadium
24 Cr Chromium
25 Mn Manganese
26 Fe Iron
27 Co Cobalt
28 Ni Nickel
rel_SO
rel_MoE
rel_MoC
all

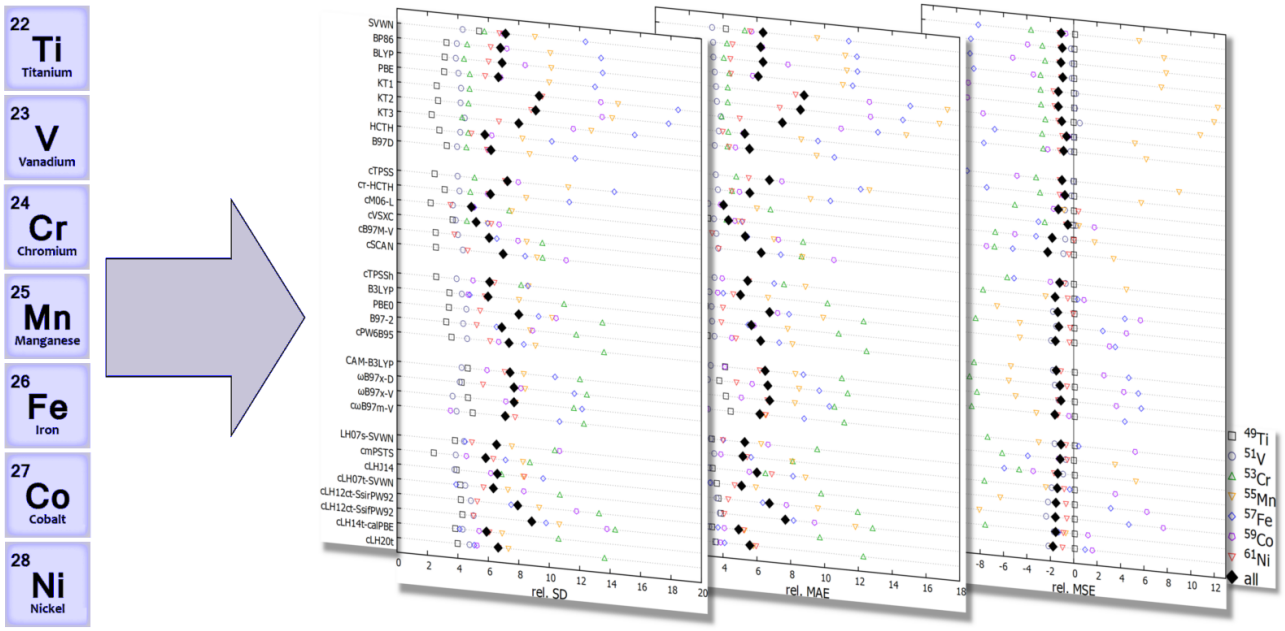
22 Ti Titanium
23 V Vanadium
24 Cr Chromium
25 Mn Manganese
26 Fe Iron
27 Co Cobalt
28 Ni Nickel
SVWN
BP86
BLYP
PBE
KT1
KT2
KT3
HCTH
B97D
cTPSS
cτ-HCTH
cM06-L
cVSXC
cB97M-V
cSCAN
cTPSSh
B3LYP
PBE0
B97-2
cPW6B95
CAM-B3LYP
ωB97x-D
ωB97x-V
ωB97m-V
LH07s-SVWN
cmPSTS
cLHJ14
cLH07t-SVWN
cLH12ct-SsirPW92
cLH12ct-SsifPW92
cLH14t-calPBE
cLH20t
rel. SD
rel. MAE
rel. MSE
49Ti
51V
53Cr
55Mn
57Fe
59Co
61Ni
all